

Solar–System Experiments in the Search for Dark Energy and Dark Matter

Slava G. Turyshev

*Jet Propulsion Laboratory, California Institute of Technology,
4800 Oak Grove Drive, Pasadena, CA 91109-0899, USA*

(Dated: September 9, 2025)

We reassess the realistic discovery reach of Solar–System experiments for dark energy (DE) and dark matter (DM) and quantify their complementarity to dedicated cosmological probes, such as the Dark Energy Spectroscopic Instrument (DESI) and Euclid mission. In scalar-tensor frameworks with universal conformal coupling $A(\phi)$, screening (chameleon/symmetron, Vainshtein) suppresses fifth forces in deep Solar potentials, consistent with the gravitational-wave speed bound $|c_T/c - 1| \lesssim 10^{-15}$. We treat Solar–System tests as hypothesis-driven probes: we assemble quantitative guardrails (MICROSCOPE η , Cassini γ , LLR \dot{G}/G and SEP, ephemeris limits on ρ_{DM} and Yukawa $\alpha(\lambda)$, and clock-network searches for ultralight DM), place them alongside current cosmology posteriors, and provide an explicit map from cosmology-level linear response (e.g., $\mu_{\text{lin},0}$) to local residuals using the screening relations (thin-shell and Vainshtein). Guided by systematics-gated criteria, we outline a near-term program—solar-conjunction Shapiro-delay and Doppler/range tests, sustained millimeter-class LLR, global optical-clock links, refined ephemerides, and spaceborne atom interferometry (AIS)—with realistic sensitivities $|\gamma - 1| \in (2-5) \times 10^{-6}$, $\eta_{\text{EEP}} \sim 10^{-16}-10^{-17}$ (AIS/LLR), $|\dot{G}/G| \lesssim (2-5) \times 10^{-14} \text{ yr}^{-1}$, a uniform $\simeq 2\times$ tightening of AU-scale Yukawa/DM-density bounds, and $3-10\times$ gains in ultralight-DM couplings from clock networks. Primary discovery potential for late-time dark energy lies with multi-probe cosmology (geometry and growth), while a hypothesis-driven Solar–System program supplies high-leverage falsification and selective discovery windows for dark matter with ultralight mediators or long-range forces.

I. INTRODUCTION AND SCOPE

Connecting predictions made at cosmological mean densities, $\bar{\rho} \sim 10^{-29} \text{ g cm}^{-3}$, to Solar–System environments spanning (i) near-Sun interplanetary plasma along conjunction rays with $\rho \sim 10^{-22}-10^{-19} \text{ g cm}^{-3}$, and (ii) bulk planetary/stellar matter with $\rho \sim 1-10^2 \text{ g cm}^{-3}$, requires a controlled theoretical bridge. In scalar–tensor theories with a universal (conformal) matter coupling $A(\phi)$, one introduces the environment-dependent effective potential

$$V_{\text{eff}}(\phi; \rho) \equiv V(\phi) + \rho A(\phi), \quad \left. \frac{dV_{\text{eff}}}{d\phi} \right|_{\phi_*} = V'(\phi_*) + \rho A'(\phi_*) = 0, \quad (1)$$

so that the ambient density selects $\phi_*(\rho)$ and hence the local coupling ($'$ denotes $d/d\phi$); ρ is the Jordan–frame rest–mass density. Screening mechanisms—chameleon and symmetron (potential/threshold screening) and Vainshtein or other derivative screening—were developed to reconcile cosmic acceleration or modified growth with stringent small-scale tests [1–5]. The multimessenger observations of the gravitational-wave (GW) event GW170817 and the gamma-ray-burst (GRB) counterpart GRB170817A imply that the tensor propagation speed, c_T , must agree with that of light to high precision, $|c_T/c - 1| \lesssim 10^{-15}$, thereby eliminating broad model classes or pushing them toward general relativity (GR)-like limits on large scales [6–10].

In what follows, Solar–System tests are treated as hypothesis-driven probes rather than model-blind searches. Specifically, we require (i) a specified microphysical model¹ (a concrete mediator and couplings) that fixes $\{V(\phi), A(\phi)\}$ in scalar-tensor theories, or the corresponding coupling structure for dark matter; and (ii) at least one forecasted local signature—such as a target for $\gamma - 1$, $\beta - 1$, \dot{G}/G , a Yukawa amplitude $\alpha(\lambda)$, or a clock modulation tied to the Einstein equivalence principle (EEP)—that exceeds a credible threshold given Solar–System gravitational potentials. When these conditions are met, the resulting measurements function as decisive tests.

To avoid unconstrained function fitting, we adopt minimal theoretical assumptions standard for low-energy long-range sectors: (1) effective field theory (EFT) locality and analyticity with approximate symmetries controlling small parameters; (2) radiative stability (technical naturalness) of light fields and couplings; (3) positivity and causality bounds compatible with a healthy ultraviolet (UV) completion (e.g., amplitude-positivity constraints [11]); (4) consistency of the adopted screening mechanism across Newtonian gravitational potentials $\Phi_N \sim 10^{-11}-10^{-6}$ relevant to Solar–System bodies (see Table I); and (5) the GW speed constraint quoted above.

¹ Terminology: Throughout, a specified microphysical model means an explicit dark-sector hypothesis with fixed low-energy dynamics. In scalar–tensor frameworks this corresponds to a concrete pair $\{V(\phi), A(\phi)\}$; for dark matter it corresponds to an explicit coupling structure or operator.

TABLE I. Surface Newtonian potentials $\Phi_N \equiv GM/(Rc^2)$ (dimensionless) relevant for screening.

Body	Mass	Φ_N
Sun	M_\odot	2.12×10^{-6}
Jupiter	$9.55 \times 10^{-4} M_\odot$	1.9×10^{-8}
Earth	$3.00 \times 10^{-6} M_\odot$	6.96×10^{-10}
Moon	$3.69 \times 10^{-8} M_\odot$	3.14×10^{-11}

For canonical parameters placing $r_{V\odot} \sim 10^2$ pc, the Vainshtein residual scales as $(r/r_V)^{3/2}$, giving $\delta F/F \lesssim 10^{-10}$ at 1 AU—explaining why PPN signatures can be null even if cosmology shows percent-level growth anomalies. At $r = 1$ AU and $r_{V\odot} \simeq 1.2 \times 10^2$ pc, this yields $\delta F/F \sim (1 \text{ AU}/120 \text{ pc})^{3/2} \sim 10^{-11}$. Under these assumptions, screening does not erase all effects; it leaves residual, environment-dependent signatures that are calculable and therefore falsifiable in Solar–System settings [4, 5]. These priors restrict admissible low-energy couplings but do not uniquely determine $A(\phi)$. For forecasts we adopt the canonical conformal form $A(\phi) = \exp(\chi\phi/M_{\text{Pl}})$, motivated by radiative stability and a universal matter coupling; other analytic choices map to the same leading predictions with χ reinterpreted as the local slope $A'(\phi_*)/A(\phi_*)$. Note that here and below we take $\chi \equiv M_{\text{Pl}} \partial \ln A / \partial \phi$ evaluated at the ambient field value ϕ_* set by the local density, i.e. the *dimensionless* coupling; thus $\partial \ln A / \partial \phi = \chi/M_{\text{Pl}}$ for $A(\phi) = \exp(\chi\phi/M_{\text{Pl}})$. When we write “ $\chi = \text{const}$ ”, interpret this as the local slope $A'(\phi_*)/A(\phi_*)$ appropriate for the observable under consideration.

The scope of this work is accordingly limited to three questions: whether Solar–System experiments (i) provide incisive model-agnostic guardrails—principally the EEP, the parameterized post-Newtonian (PPN) framework, and bounds on \dot{G}/G ; (ii) exclude unscreened or weakly screened regions of theory space; and (iii) open credible discovery windows for concrete dark-sector hypotheses, for example ultralight scalar or vector dark matter (DM). We answer (i)–(iii) in the affirmative, noting that late-time dark-energy dynamics are most likely to be identified first by cosmological probes (e.g., the Dark Energy Spectroscopic Instrument (DESI)², Euclid³), that jointly constrain geometry and growth [12–16].

Our analysis yields an important programmatic recommendation: Authorize a dedicated Solar–System mission only when a specified microphysical model (with explicit $\{V(\phi), A(\phi)\}$ or dark-sector couplings) predicts at least one local signature— $|\gamma - 1|$, $|\beta - 1|$, \dot{G}/G , a Yukawa $\alpha(\lambda)$, or a clock/AIS modulation—exceeding credible detection thresholds given Solar potentials Φ_N . Otherwise, support dedicated efforts including piggybacked radio/optical links, LLR, clock networks, and ephemeris improvements and reprocessing.

The structure of this paper is as follows. Section I sets the theoretical priors (screening, EFT/positivity, GW-speed bound) and scope. Section II develops the bridge from cosmological to local phenomenology, including thin-shell and Vainshtein numerics. Section III reviews current Solar–System bounds and credible near-term targets (EEP, PPN γ, β , \dot{G}/G , Yukawa tails, ultralight-DM clocks, and atom interferometer in space (AIS)). Section IV summarizes DESI/Euclid constraints and demonstrates the two-stage mapping—with a worked example—from μ_0^{lin} to local residuals. Section V lays out a targeted near-term program (radio/optical conjunctions, mm-class LLR, optical clock links, and ephemerides) with a risk register and a decision rule for dedicated missions. Section VI closes with the asymmetric strategy—cosmology for discovery; Solar–System tests for guardrails and selective DM discovery—while Appendices A–B extend the guardrails to disformal couplings and provide a toy cross-regime likelihood. Appendix C provides a step-by-step roadmap that collects the assumptions, equations, and data products used throughout. Appendix D demonstrates that the Sun’s thin-shell behavior yields a PPN- γ compatible with Cassini constraints.

II. THEORY BRIDGE AND SCREENING NUMERICS

For chameleon-like screening, consider a spherical body of mass M , radius R , and surface Newtonian potential $\Phi_N \equiv GM/(Rc^2)$, see Table II for notations. In an ambient environment where the scalar field takes the value ϕ_∞ ,

² For details on the Dark Energy Spectroscopic Instrument (DESI), see <https://www.desi.lbl.gov/>

³ For details on the ESA’s Euclid mission, see https://www.esa.int/Science_Exploration/Space_Science/Euclid

TABLE II. Notation summary (symbols used most often in the text).

Symbol	Meaning
M_{Pl}	reduced Planck mass
$\Phi_N \equiv GM/(Rc^2)$	surface Newtonian potential
$A(\phi) = \exp(\chi\phi/M_{\text{Pl}})$	conformal matter coupling; $\chi \equiv M_{\text{Pl}} \partial \ln A / \partial \phi _{\phi_\star}$
$\mu(z, k), \Sigma(z, k)$	linear-response functions for clustering and lensing
$\mu_{\text{lin},0}$	shorthand $\mu(z=0, k_{\text{fid}}) - 1$ with $k_{\text{fid}} \simeq 0.1 h \text{ Mpc}^{-1}$
$r_S = 2GM/c^2$	Schwarzschild radius; r_V Vainshtein radius
α_Y, λ	Yukawa strength and range ($m = \hbar c/\lambda$)
t_c	ULDM coherence time $t_c \simeq 2\pi/(m_\phi v^2)$
AU	astronomical unit

while inside the body it relaxes to ϕ_c , the object develops a thin shell of fractional thickness⁴

$$\frac{\Delta R}{R} \simeq \frac{\phi_\infty - \phi_c}{6 \chi M_{\text{Pl}} \Phi_N}, \quad (2)$$

where χ is the dimensionless matter coupling and M_{Pl} is the reduced Planck mass.

Eq. (2) assumes a screened source with a *thin* shell, $\Delta R/R \ll 1$. When $\Delta R/R$ approaches unity, the screened-source premise fails and the γ -mapping in Eq. (22) no longer applies; such parameter points are automatically excluded by Solar-System bounds (cf. Appendix D).

For the benchmark potential $V(\phi) = \Lambda^{4+n}\phi^{-n}$ with $A(\phi) = e^{\chi\phi/M_{\text{Pl}}}$, the density-dependent minimum solves $V'(\phi_\star) + \rho A'(\phi_\star) = 0$, giving

$$\phi_\star(\rho) = \left(\frac{n \Lambda^{4+n} M_{\text{Pl}}}{\chi \rho} \right)^{\frac{1}{n+1}}, \quad (3)$$

where we used $A(\phi_\star) \simeq 1$ for $\chi \phi_\star/M_{\text{Pl}} \ll 1$ (equivalently, interpret χ as the local slope $A'(\phi_\star)/A(\phi_\star)$). Substituting $\phi_\infty = \phi_\star(\rho_\infty)$ and $\phi_c = \phi_\star(\rho_c)$ in (2) yields an explicit (n, Λ, χ) dependence for the thin shell:

$$\frac{\Delta R}{R} \simeq \frac{\phi_\star(\rho_\infty) - \phi_\star(\rho_c)}{6 \chi M_{\text{Pl}} \Phi_N}. \quad (4)$$

In the Sun-screened regime ($\rho_c \gg \rho_\infty$ so $\phi_c \ll \phi_\infty$), this simplifies to $\Delta R/R \simeq \phi_\star(\rho_\infty)/(6 \chi M_{\text{Pl}} \Phi_N)$.

We model the near-Sun interplanetary medium along conjunction rays as log-normal, $\ln \rho_\infty \sim \mathcal{N}(\ln \rho_0, \sigma_{\ln \rho}^2)$ with $\rho_0 = 10^{-20} \text{ g cm}^{-3}$ and $\sigma_{\ln \rho} = \ln 10$ (one-decade 1σ), consistent with Table III. For the power-law chameleon in (3), $\Delta R/R \propto \rho_\infty^{-1/(n+1)}$, so uncertainties propagate as $\sigma_{\ln(\Delta R/R)} = \sigma_{\ln \rho}/(n+1)$. Throughout we adopt the conservative prior $\rho_\infty \in [10^{-22}, 10^{-19}] \text{ g cm}^{-3}$ “a few R_\odot ” from the Sun and report sensitivities as explicit power laws in ρ_∞ (Table III).

Note that for forecasting purposes, we adopt a fiducial interplanetary medium near conjunction $\rho_\infty \equiv \rho_{\text{IPM}} \in [10^{-22}, 10^{-19}] \text{ g cm}^{-3}$ (consistent with proton densities $n_p \sim 10^2\text{--}10^5 \text{ cm}^{-3}$ at a few R_\odot), and we present bounds as explicit power laws in ρ_∞ , that for the power-law chameleon $V(\phi) = \Lambda^{4+n}\phi^{-n}$ and universal conformal coupling $A(\phi) = \exp[\chi\phi/M_{\text{Pl}}]$, take the form

$$\left(\frac{\Delta R}{R} \right)_{\rho_\infty} \propto \rho_\infty^{-1/(n+1)}, \quad \Lambda^{4+n}(\rho_\infty) \lesssim \frac{\chi}{n M_{\text{Pl}}} \rho_\infty \left[M_{\text{Pl}} \Phi_{N\odot} \sqrt{|\gamma - 1|_{\text{max}}} \right]^{n+1}.$$

Thus, one can rescale Eqs. (23)–(26) below to any preferred ρ_∞ without re-deriving intermediate steps. As a result, this yields the compact rescaling form of the bound derived from the thin-shell relation and the Shapiro-delay null test (cf. Eqs. (23) and (24) below).

⁴ Conventions: We keep c and \hbar explicit unless otherwise stated; where dimensionless normalizations are standard (e.g., $\Phi_N \equiv GM/(Rc^2)$), we follow conventional astrophysical units. We use the reduced Planck mass $M_{\text{Pl}} \equiv 1/\sqrt{8\pi G}$. Throughout the paper the scalar field carries its canonical mass dimension, $[\phi] = \text{mass}$. We define the *dimensionless* conformal matter coupling (possibly composition-dependent) evaluated at the ambient field value ϕ_\star as

$$\chi(\phi) \equiv M_{\text{Pl}} \left(\frac{\partial \ln A(\phi)}{\partial \phi} \right) \Big|_{\phi_\star},$$

so that when $A(\phi) = \exp[\chi\phi/M_{\text{Pl}}]$ with constant χ , the local slope is $(\partial \ln A / \partial \phi)_{\phi_\star} = \chi/M_{\text{Pl}}$. Throughout the text we use the symbol χ for this dimensionless coupling. With this convention Eqs. (2)–(7) and (21)–(24) are dimensionally consistent and coincide with the standard chameleon notation. Also, for a universal coupling one has $\chi_A = \chi_B = \chi$.

TABLE III. Effect of the ambient-density prior on the thin-shell bound for a power-law chameleon (n shown). Entries show the multiplicative rescaling of $(\Delta R/R)_{\max}$ relative to a reference $\rho_{\infty,0} = 10^{-20} \text{ g cm}^{-3}$. Because $\Delta R/R \propto \rho_{\infty}^{-1/(n+1)}$ for the power-law chameleon in (3), the entries equal $(\rho_{\infty}/\rho_{\infty,0})^{-1/(n+1)}$ for the listed n values.

n	$\rho_{\infty} = 10^{-22}$	10^{-20} (ref.)	10^{-19}
1	$(10^{-22}/10^{-20})^{-1/2} = 10$	1	$(10^{-19}/10^{-20})^{-1/2} = 0.316$
2	$(10^{-22}/10^{-20})^{-1/3} = 4.64$	1	$(10^{-19}/10^{-20})^{-1/3} = 0.464$
3	$(10^{-22}/10^{-20})^{-1/4} = 3.16$	1	$(10^{-19}/10^{-20})^{-1/4} = 0.562$

For a compact source A and test body B , the scalar-mediated force relative to Newtonian gravity may be written in a form that makes the screening of each body explicit:

$$\frac{F_{\phi}}{F_N} = 2\chi_A\chi_B \times \begin{cases} 1, & A \text{ and } B \text{ both unscreened,} \\ 3\Delta R_A/R_A, & A \text{ screened, } B \text{ unscreened,} \\ 3\Delta R_B/R_B, & A \text{ unscreened, } B \text{ screened,} \\ 9(\Delta R_A/R_A)(\Delta R_B/R_B), & A \text{ and } B \text{ both screened.} \end{cases} \quad (5)$$

In particular, for an *unscreened* test mass B outside a screened spherical source A , the scalar-mediated force is suppressed relative to Newtonian gravity by

$$\frac{F_{\phi}}{F_N} \simeq 2\chi^2 \min\left(1, \frac{3\Delta R}{R}\right), \quad (6)$$

with $\chi_A = \chi_B = \chi$ for a universal coupling. As a result, screened objects with $\Delta R/R \ll 1$ source only a small residual fifth force [1, 2, 4]. Numerically,

$$\Phi_N \simeq 2.12 \times 10^{-6} \text{ (Sun)}, \quad 6.96 \times 10^{-10} \text{ (Earth)}, \quad 3.14 \times 10^{-11} \text{ (Moon)}, \quad (7)$$

which quantifies why inner-Solar-System bodies are typically deep in the screened regime unless parameters lie near screening boundaries (see Appendix C for more discussion on the relevant conditions.)

Below, we use $\Phi_N \equiv GM/(Rc^2)$ for surface Newtonian potentials; screening via Eqs. (2)–(7) (chameleon-like) and Eqs. (10)–(11) (Vainshtein-like); and the linear-response MG parameters $\mu(z, k)$ and $\Sigma(z, k)$ with $\mu_0^{\text{lin}} \equiv \mu(z=0, k \sim 0.1 \text{ h Mpc}^{-1}) - 1$. When an explicit coupling is required for a forecast, we use $A(\phi) = \exp(\chi\phi/M_{\text{Pl}})$. In the unscreened regime this implies $\mu \simeq 1 + 2\chi^2$ and hence $\chi \simeq \sqrt{\mu_0^{\text{lin}}/2}$ [Eq. (21)]. This choice is for definiteness and does not imply uniqueness.

In Newtonian gauge ($ds^2 = -(1 + 2\Psi)dt^2 + a^2(1 - 2\Phi)d\mathbf{x}^2$), we define

$$-k^2\Psi = 4\pi G a^2 \mu(z, k) \rho_m \Delta_m, \quad (8)$$

$$-k^2(\Phi + \Psi) = 8\pi G a^2 \Sigma(z, k) \rho_m \Delta_m, \quad (9)$$

so that μ rescales clustering (motion in Ψ) and Σ rescales light deflection. In the conformal benchmark with negligible linear anisotropic stress (so $\Phi \simeq \Psi$), Σ tracks μ up to $\mathcal{O}(1)$ factors; we therefore quote $\mu_0^{\text{lin}} \equiv \mu(z=0, k_{\text{fid}}) - 1$ as the primary cosmology→local bridge parameter.

Remark on scale. Unless otherwise stated, we evaluate $\mu_0^{\text{lin}} \equiv \mu(z=0, k) - 1$ at the representative linear scale $k_{\text{fid}} \simeq 0.1 \text{ h Mpc}^{-1}$. Mappings from μ_0^{lin} to local residuals therefore inherit a mild k -dependence through $\mu(z, k)$; results quoted here should be read as band-limited around k_{fid} .

In chameleon-like models the scalar Compton wavelength $\lambda_c(\rho) = m_{\phi}^{-1}(\rho)$ sets a mild k -dependence in $\mu(z, k)$ through the transition between screened ($k\lambda_c \ll 1$) and unscreened ($k\lambda_c \gg 1$) linear modes. Our choice $k_{\text{fid}} \simeq 0.1 \text{ h Mpc}^{-1}$ lies within the band where DESI/Euclid have the highest signal, and our mapping should be read as band-limited around k_{fid} ; translating to nearby k requires the standard linear response $\mu(z, k)$ of the chosen microphysical model.

Derivative (Vainshtein) screening suppresses fifth forces outside a characteristic Vainshtein radius r_V set by nonlinear kinetic interactions. We take the cross-over scale $r_c \equiv c/H_0$ in DGP-like models (with H_0 the Hubble constant), so for canonical cases one finds scaling relations of the form

$$r_V \sim (r_S r_c^2)^{1/3} \quad (\text{DGP-like}), \quad r_V \sim \left(\frac{r_S}{\Lambda^3}\right)^{1/3} \quad (\text{cubic Galileon-like}), \quad (10)$$

where $r_S \equiv 2GM/c^2$ is the Schwarzschild radius, r_c is the cross-over scale (of order c/H_0 in DGP), and Λ is the strong-coupling scale of the Galileon sector [5]. For illustration, taking $r_c \simeq c/H_0$ gives

$$r_V \simeq 1.2 \times 10^2 \text{ pc (Sun)}, \quad r_V \simeq 1.7 \text{ pc (Earth)}, \quad (11)$$

placing the entire Solar System well inside the Vainshtein region and strongly suppressing leading deviations from GR.

These screening mechanisms explain why many fully relativistic dark-energy models predict negligible parameterized post-Newtonian deviations locally, while still allowing cosmological signatures in the background expansion, growth, or lensing—subject to the gravitational-wave speed bound $|c_T/c - 1| \lesssim 10^{-15}$ [8, 9].

III. SOLAR-SYSTEM OBSERVABLES: STATUS AND CREDIBLE IMPROVEMENTS

We summarize present leading bounds, the physics they probe, and realistic near-term gains under concrete measurement conditions (see Tables V and VI for details). Some of the relevant reviews are given in [17, 18].

A. Einstein equivalence principle and composition dependence

The Eötvös parameter $\eta_{\text{EEP}}(A, B) \equiv 2(a_A - a_B)/(a_A + a_B)$ quantifies differential acceleration of test bodies A and B in the same external field. The MICROSCOPE mission compared titanium and platinum proof masses and reported [19]

$$\eta_{\text{EEP}}(\text{Ti, Pt}) = (-1.5 \pm 2.3_{\text{stat}} \pm 1.5_{\text{syst}}) \times 10^{-15}, \quad (12)$$

which excludes many unscreened scalar-tensor couplings and severely restricts dilaton-type models.

A purpose-built follow-on or a dedicated, drag-free, space atom interferometer such as Space-Time Explorer and QUantum Equivalence principle Space Test (STE-QUEST)-class atom-interferometer mission can credibly improve sensitivity by one order of magnitude, reaching $\eta_{\text{EEP}} \sim 10^{-16}$ – 10^{-17} , using long interrogation times T , dual/multi-species comparisons, and common-mode rejection [20, 21]. We therefore treat AIS primarily as a precision EEP instrument (a universal guardrail) rather than a generic DE-discovery probe, consistent with our hypothesis-driven strategy.

B. Parameterized post-Newtonian gravity: γ and β

In the parameterized post-Newtonian (PPN) framework, γ measures spatial curvature per unit mass and β encodes nonlinearity in superposition [22]. The Shapiro time delay provides access to PPN γ via

$$\Delta t \simeq (1 + \gamma) \frac{GM_\odot}{c^3} \ln\left(\frac{4r_E r_R}{b^2}\right), \quad (13)$$

where r_E and r_R are the heliocentric distances of emitter and receiver, and b is the impact parameter of the radio path. The 2002 solar-conjunction experiment with Cassini spacecraft obtained [23]

$$\gamma - 1 = (2.1 \pm 2.3) \times 10^{-5}. \quad (14)$$

The dependence of the 1σ sensitivity to $|\gamma - 1|$ on solar impact parameter is shown in Fig. 1(b), with Cassini's 2.3×10^{-5} reference and the 10^{-6} target. As we show in Appendix D, for chameleon-like benchmarks, the Sun thin-shell mapping implies that a factor of ~ 2 – 4 improvement over the current $|\gamma - 1|$ sensitivity would directly probe the predicted residuals (see the ρ_∞ scaling summarized in Table III and the guardrail in (23)).

In global ephemerides, β is constrained in combination with γ through perihelion precession and solar-system dynamics. For a test body with (a, e) one has the PPN perihelion shift per orbit

$$\Delta\varpi = \frac{1}{3}(2 + 2\gamma - \beta) \frac{6\pi GM_\odot}{a(1 - e^2)c^2}, \quad (15)$$

so Ka/X multi-frequency conjunction arcs that tighten γ also reduce degeneracies in (15), improving β in the subsequent global fits.

Dual-frequency Ka/X calibration mitigates coronal plasma dispersion, while accelerometry and thermal modeling bound non-gravitational forces; with optimized conjunction arcs this supports $\sigma_\gamma \sim \text{few} \times 10^{-6}$. The Mercury Orbiter Radio-science Experiment (MORE) on *BepiColombo* aims at γ at the level of a $\text{few} \times 10^{-6}$ using Ka/X multi-frequency links, improved coronal-plasma calibration, and optimized conjunction arcs, with comparable sensitivity to β in global ephemeris fits [24, 25]. These remain among the cleanest astronomical-unit (AU) scale tests of long-range metric gravity.

Considering optical links we note that the DSOC tech demo established deep-space coherent optical links with a peak downlink of 267 Mbs^{-1} at $\sim 0.2 \text{ AU}$ (Dec. 11, 2023), and sustained 25 Mbs^{-1} at $\sim 1.5 \text{ AU}$ (Apr. 8, 2024), validating pointing, acquisition, and timing needed for precision relativistic tests [26–28]. We model coronal plasma dispersion with the standard group delay

$$\Delta t_{\text{plasma}} \simeq 40.3 \frac{\text{TEC}}{cf^2} \text{ s}, \quad (16)$$

where f is the carrier frequency (Hz) and TEC the electron column density (m^{-2}). The normalization in Eq. (16) follows the standard cold-plasma dispersion law used in radio science, and underlies the f^{-2} scaling. As a result, (16) gives a *time* delay; the corresponding group path delay is $\Delta L_{\text{plasma}} = c \Delta t_{\text{plasma}} = 40.3 \text{ TEC}/f^2$ (m). The optical suppression factors quoted below follow directly from the f^{-2} scaling.

At optical $f \sim 2 \times 10^{14} \text{ Hz}$, the suppression relative to X-band (8.4 GHz) is $(8.4 \times 10^9 / 2 \times 10^{14})^2 \approx 1.76 \times 10^{-9}$ and to Ka-band (32 GHz) is $(3.2 \times 10^{10} / 2 \times 10^{14})^2 \approx 2.56 \times 10^{-8}$. Thus optical links reduce coronal group-delay systematics by $\mathcal{O}(10^8 - 10^9)$ vs. current radio bands. As summarized in Fig. 1(a), the residual group delay scales as f^{-2} ; Ka and especially optical links strongly suppress coronal dispersion relative to X.

To reach $|\gamma - 1| \sim \text{few} \times 10^{-6}$ at $b \gtrsim 5 R_\odot$ we allocate the post-calibration group-delay budget to $\leq 0.1 \text{ ns}$ [Table VII], split as: plasma/turbulence (40 ps; already suppressed as f^{-2} per Fig. 1a), non-gravitational forces and thermal/attitude coupling (30 ps over a 10-day dwell), and timing/transfer chain (30 ps). This allocation tracks the frequency scaling in (16) and the pointing/thermal constraints quoted in Sec. V, and serves as the nuisance floor drawn in Fig. 1b.

Figure 1 summarizes the inputs used in the forecasts: Panel (a) shows the X-normalized residual group delay versus carrier frequency f [Hz], following the coronal dispersion law (16). Panel (b) gives the 1σ sensitivity to $|\gamma - 1|$ as a function of the solar impact parameter b/R_\odot , set by the Shapiro time delay (13) against the calibrated residual noise; reference lines at Cassini 2.3×10^{-5} and the 1×10^{-6} target are indicated. Panel (c) maps a null γ bound into a maximum solar thin-shell fraction $\Delta R/R$ as a function of $\mu_{\text{lin},0}$ using (21)–(24). Panel (d) summarizes the normalized clock sensitivity to an α -coupled coefficient d_e versus m_ϕ [eV] from the coherence-time/bandwidth scalings (Eqs. (18)–(19)); “current” and “advanced links/stability” reflect the link-noise and integration assumptions used in the analysis. Although not plotted, the AIS EEP channel enters the same screening map via Eq. (20), supplying an Earth-thin-shell guardrail complementary to the Sun-thin-shell bound in panel (c).

C. Time variation of G and the strong-equivalence principle

Lunar Laser Ranging (LLR) constrains the fractional time variation of Newton’s constant and the Nordtvedt parameter (a strong-equivalence-principle, SEP, violation). Early global analyses reported $|\dot{G}/G| \sim 10^{-13} \text{ yr}^{-1}$ and SEP at $\eta_{\text{SEP}} = 4\beta - \gamma - 3 - \frac{10}{3}\xi - \alpha_1 - \frac{2}{3}\alpha_2 \sim 10^{-4}$ class [29]. In minimal scalar–tensor completions the preferred-frame and Whitehead parameters are negligible, so $\eta_{\text{SEP}} \approx 4\beta - \gamma - 3$. Ephemerides directly constrain GM_\odot ; separating \dot{G} from solar mass loss requires solar-physics priors.

Modern ephemerides and LLR combinations give $|\dot{G}/G|$ in the $(2\text{--}6) \times 10^{-14} \text{ yr}^{-1}$ range [30, 31]. Millimeter-class LLR with next-generation corner-cube retroreflectors (CCR), improved station metrology, and higher link budgets can plausibly strengthen these bounds by a factor $\sim 2\text{--}3$ [32]. Recent LLR global solutions already constrain $\Delta(m_g/m_i)_{\text{EM}} = (-2.1 \pm 2.4) \times 10^{-14}$ and $\dot{G}/G_0 = (-5.0 \pm 9.6) \times 10^{-15} \text{ yr}^{-1}$ [33]; next-generation IR stations and single-CCR deployments are expected to tighten both.

Note that in universally coupled, screened scalar models, Solar–System bodies acquire suppressed scalar charges through the thin-shell relation (2)–(7). The Nordtvedt/SEP signal in the Earth–Moon system depends on the *difference* of Earth/Moon charges in the Sun’s *screened* field η_{SEP} and is therefore doubly thin-shell and composition suppressed. Present LLR SEP bounds are complementary but do not overtake conjunction constraints on γ in this class; sub-mm LLR with range precision of $\sim 30 \mu\text{m}$ [32] can strengthen η_{SEP} and \dot{G}/G by $\sim 3\text{--}7\times$ and sharpen β in global fits (Table V; Table VII).

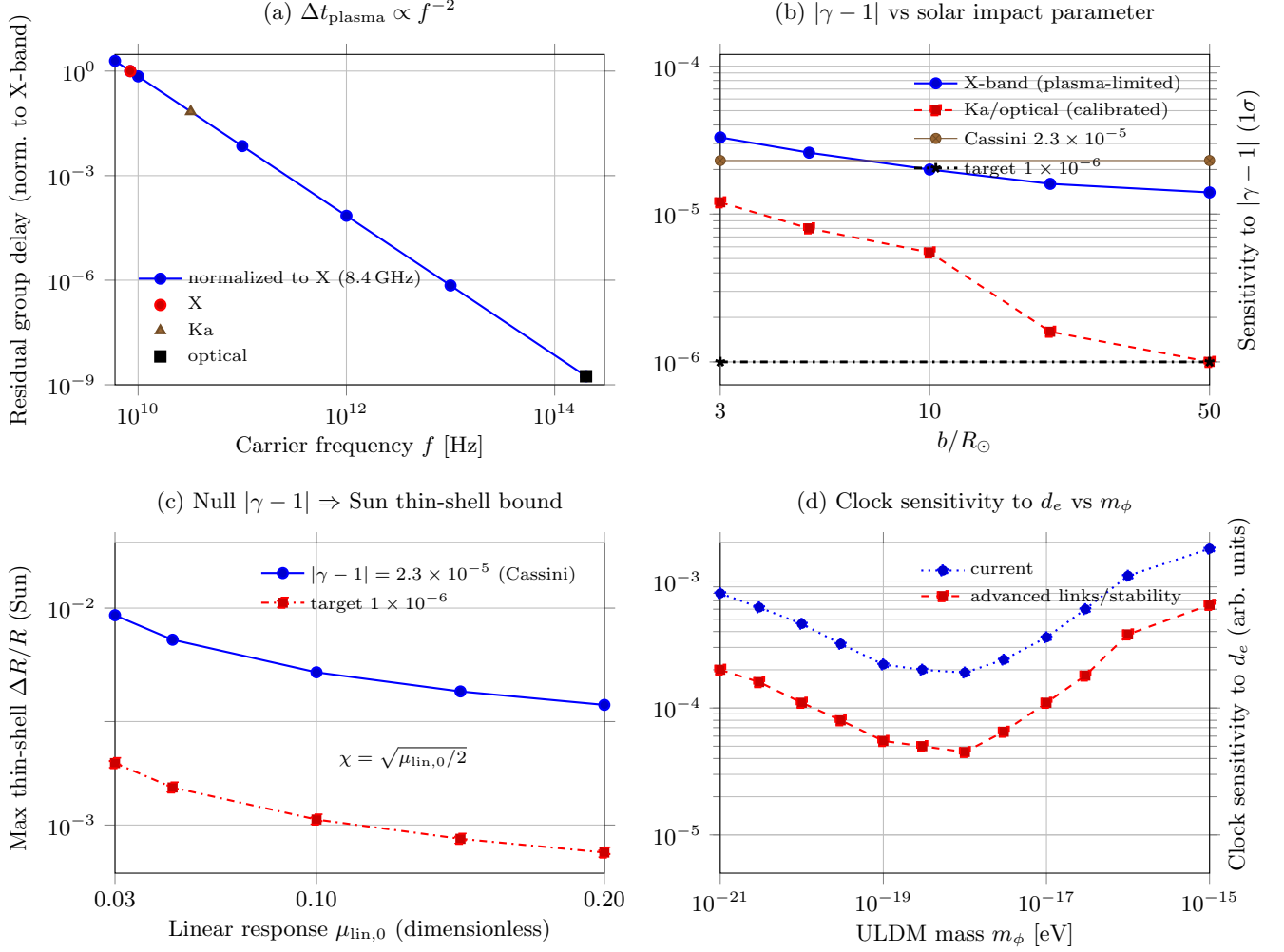


FIG. 1. Solar-System sensitivities with advanced links and analysis. (a) Residual plasma group delay (normalized to X-band) versus carrier frequency f (Hz), following the f^{-2} law in Eq. (13). (b) 1σ sensitivity to $|\gamma - 1|$ versus solar impact parameter b/R_{\odot} , with Cassini (2.3×10^{-5}) and a 10^{-6} target for reference. Curves assume a post-calibration residual time-delay budget ≤ 0.1 ns for $b \gtrsim 5 R_{\odot}$ (40 ps plasma/turbulence, 30 ps non-gravitational, 30 ps timing/transfer). (c) Maximum solar thin-shell fraction $\Delta R/R$ implied by a null $|\gamma - 1|$ bound, as a function of the cosmology-level response $\mu_{\text{lin},0}$, using Eqs. (21)–(23). (d) Normalized clock sensitivity to an α -coupled coefficient d_e versus m_{ϕ} from the coherence-time/bandwidth scalings, Eqs. (18)–(19), clock sensitivity to d_e (arbitrary units).

D. Solar-System dark-matter density and Yukawa tails

Global ephemeris fits limit any smoothly distributed dark matter (DM) in the Solar System. At Saturn’s orbit one finds $\rho_{\text{DM}} \lesssim 1.1 \times 10^{-20} \text{ g cm}^{-3}$, with mass enclosed within Saturn’s orbit $< 8 \times 10^{-11} M_{\odot}$ [34–36]. The same datasets constrain Yukawa deviations of the form

$$V(r) = -\frac{GMm}{r} \left[1 + \alpha_Y e^{-r/\lambda} \right], \quad (17)$$

where α is the strength and λ the range. We convert range to mass via

$$m \equiv \frac{\hbar c}{\lambda} \simeq \frac{1.97327 \times 10^{-7} \text{ eV} \cdot \text{m}}{\lambda},$$

where Table IV shows representative parameters. From (17), Yukawa acceleration takes the form

$$a_Y(r) = -\frac{GM}{r^2} \alpha \left(1 + \frac{r}{\lambda} \right) e^{-r/\lambda},$$

TABLE IV. Mediator mass–range map, $m = \hbar c/\lambda$.

Range λ (m)	m (eV)	Comment
10^9	1.97×10^{-16}	inner Solar–System scale
10^{11}	1.97×10^{-18}	AU scale
10^{13}	1.97×10^{-20}	multi–AU scale

so AU-scale sensitivities peak for $\lambda \sim 10^9\text{--}10^{13}$ m (i.e., mediator masses $m \equiv \hbar c/\lambda \simeq 2 \times 10^{-16}\text{--}2 \times 10^{-20}$ eV), with small-body/spacecraft tracking now providing leading bounds in parts of this band.

Across $\lambda \in [10^9, 10^{13}]$ m, current ephemerides and small-body/spacecraft tracking deliver leading bounds $|\alpha_Y| \ll 10^{-9}\text{--}10^{-10}$ (depending on λ , data selection, and solar-plasma modeling [31]), and we assume a uniform factor-of-two tightening across this band (Tables V, VII).

E. Ultralight dark matter (ULDM): precision clocks and interferometers

Coherently oscillating scalar DM induces variations of fundamental constants and thus fractional frequency shifts in atomic transitions,

$$\frac{\delta\nu}{\nu} \simeq \sum_i K_i d_i \phi(t), \quad (18)$$

where K_i are sensitivity coefficients, d_i coupling parameters, and ϕ the DM field. Note that in Eq. (18) we absorb the Planck suppression into the coefficients d_i , so that $[d_i] = \text{mass}^{-1}$ and $d_i \simeq \tilde{d}_i/M_{\text{Pl}}$ with \tilde{d}_i dimensionless. For a coherently oscillating scalar $\phi(t) = \phi_0 \cos(m_\phi t)$ with $\phi_0 \simeq \sqrt{2\rho_{\text{DM}}}/m_\phi$, taking $\rho_{\text{DM}} = 0.3 \text{ GeV cm}^{-3}$ and $m_\phi = 10^{-18}$ eV gives typical fractional modulations $\delta\nu/\nu \sim 10^{-19}\text{--}10^{-16}$ across plausible $K_i d_i$; space–ground optical links measurement coherence/stability and suppress environmental noise. In other words, for coherently oscillating ULDM in a virialized halo,⁵ the field coherence time is

$$t_c \simeq \frac{2\pi}{m_\phi v^2} = 4.13 \times 10^9 \text{ s} \left(\frac{10^{-18} \text{ eV}}{m_\phi} \right) \left(\frac{10^{-3}}{v/c} \right)^2. \quad (19)$$

Operationally, sensitivity *per coherence bin* saturates at t_c ; for a total campaign time T the signal-to-noise scales as $\sqrt{N_{\text{bin}}}$ with $N_{\text{bin}} \approx T/t_c$ when averaging incoherently across independent bins at fixed m_ϕ . Long-baseline optical links still enable the projected 3–10 \times coupling improvements across $m_\phi \sim 10^{-24}\text{--}10^{-15}$ eV by stabilizing the link and extending usable T , but the analysis should adopt the t_c of (19) (see [37–39].)

For a matched-filter search at fixed m_ϕ , the coherent SNR saturates over t_c and builds as $\text{SNR} \propto \sqrt{T/t_c}$ when incoherently combining $N_{\text{bin}} \simeq T/t_c$ independent coherence bins; hence the emphasis on extending T beyond t_c with stable space–ground optical links.

As an example, consider a differential comparison between transitions A and B sensitive to α with coefficients $K_\alpha^{(A)}, K_\alpha^{(B)}$, for which, from (18), the fractional beat note is

$$\left(\frac{\delta\nu}{\nu} \right)_{A/B} \simeq \Delta K_\alpha d_e \phi(t), \quad \Delta K_\alpha \equiv K_\alpha^{(A)} - K_\alpha^{(B)}.$$

Assuming a coherently oscillating field $\phi(t) = \phi_0 \cos(m_\phi t)$ with $\phi_0 \simeq \sqrt{2\rho_{\text{DM}}}/m_\phi$ and integration time T , the SNR per coherence bin is

$$\text{SNR} \sim \frac{\Delta K_\alpha |d_e| \phi_0}{\sigma_y(\tau)} \sqrt{\frac{T}{t_c}},$$

with Allan deviation $\sigma_y(\tau)$ at interrogation time τ and $t_c \simeq 2\pi/(m_\phi v^2)$ the field coherence time.

⁵ Normalization in (18)–(19): Throughout we measure ϕ in energy units (mass dimension one), so the coefficients d_i in (18) carry inverse-energy dimension and $d_i \phi$ is dimensionless. If one prefers dimensionless couplings, define $\tilde{d}_i \equiv M_{\text{Pl}} d_i$ and replace $d_i \phi \rightarrow \tilde{d}_i (\phi/M_{\text{Pl}})$. None of our sensitivities depends on this convention.

TABLE V. Representative Solar-System observables: current bounds and near-term targets under stated conditions.

Observable	Current bound	Plausible near-term target (conditions)
EEP violation η	$\sim 3 \times 10^{-15}$ (MICROSCOPE) [19]	10^{-16} – 10^{-17} with drag-free atom interferometer, multi-species comparison, and long interrogation time T [20, 21]
EEP violation (AIS)	$\sim 3 \times 10^{-15}$ (MICROSCOPE) [19]	$\eta \sim 10^{-16}$ – 10^{-17} with a drag-free space atom interferometer (dual-/multi-species, long T , high common-mode rejection) [20, 21, 44–46]
PPN $\gamma - 1$	$(2.1 \pm 2.3) \times 10^{-5}$ (Cassini, solar conjunction) [23]	$\text{few} \times 10^{-6}$ using BepiColombo/MORE Ka/X multi-frequency links, improved coronal-plasma calibration, optimized conjunction arcs; comparable sensitivity to β in global fits [24, 25]
\dot{G}/G	$\text{few} \times 10^{-14} \text{ yr}^{-1}$ from modern LLR+ephemerides [30, 31]	$\times(2\text{--}3)$ via mm-class LLR with next-generation corner-cube retroreflectors (CCRs), improved station metrology, and higher link budgets [32]
ρ_{DM} at 1–10 AU	$\lesssim 10^{-20} \text{ g cm}^{-3}$ at Saturn; enclosed mass $< 8 \times 10^{-11} M_{\odot}$ [35, 36]	$\times 2$ via long tracking arcs, Deep Space Network (DSN) reprocessing, and improved asteroid modeling in global ephemerides [31]
ULDM (clocks)	Leading limits for 10^{-24} – 10^{-15} eV from terrestrial and space-assisted clock comparisons [40, 41]	$\times(3\text{--}10)$ with space optical links and clock networks (e.g., ACES and follow-ons) to extend coherence time and suppress environmental noise [42, 43]

TABLE VI. Dominant systematics and gating improvements for each observable.

Observable	Dominant systematics	Gating improvement
γ, β (radio science)	solar plasma; non-grav. accelerations	dual-frequency calibration; long dwell times
$\dot{G}/G, \eta_{\text{SEP}}$ (LLR)	station timing/geometry; CCR thermal lensing	mm-class links; new CCRs; joint ephemerides
EEP (AIS)	gravity-gradient and magnetic backgrounds; wavefront/vibration noise	drag-free control; dual-species/common-mode rejection; gradient compensation; magnetic shielding
Yukawa/ephemerides	asteroid masses; SRP; thermal recoil	DSN reprocessing; asteroid catalogs; longer arcs
Clock DM	link noise; cavity drift; environmental couplings	space-ground optical links; multi-species networks

Terrestrial and space-assisted clock comparisons set world-leading limits over $m_{\phi} \sim 10^{-24}$ – 10^{-15} eV [40, 41]. Space segments such as the Atomic Clock Ensemble in Space (ACES) and future optical links measurement coherence/stability and suppress environmental noise, enabling new baselines and improving coupling reach by factors of ~ 3 – 10 [42, 43]. For context, Fig. 1(d) summarizes the normalized sensitivity to d_e across $m_{\phi} \in [10^{-21}, 10^{-15}] \text{ eV}$ under current and advanced link/stability assumptions.

F. Atom-interferometry in space (AIS): DE guardrails and targeted discovery

Spaceborne atom interferometers (AIs) enable long free-fall times, drag-free control, and multi-species comparisons. In the DE framing of Sec. I, their role is twofold.

Dual-species AIs (e.g., Rb/K or Sr/Rb) test the Einstein equivalence principle (EEP) via the Eötvös parameter $\eta(A, B) \equiv 2(a_A - a_B)/(a_A + a_B)$. STE-QUEST-class designs credibly reach $\eta \sim 10^{-16}$ – 10^{-17} under microgravity, long interrogation time T , and common-mode rejection [20, 21, 47]. In scalar-tensor theories with universal conformal coupling $A(\phi) = e^{\chi\phi/M_{\text{Pl}}}$, composition dependence arises when Standard-Model masses inherit distinct ϕ -sensitivities. A screened source (Earth) yields

$$\eta(A, B) \simeq 2\chi_{\oplus} \left[\min\left(1, 3 \frac{\Delta R_{\oplus}}{R_{\oplus}}\right) \right] (\chi_A - \chi_B), \quad (20)$$

so AIS limits map onto $(\chi_A - \chi_B)\chi_{\oplus}$ with the thin-shell factor from Eqs. (2)–(7). Given the cosmology→local bridge in Secs. II–IV, pushing η by 1–2 orders of magnitude sharpens guardrails on the same χ that controls $\mu(z, k)$ in linear growth (cf. Table VIII). With $A(\phi) = e^{\chi\phi/M_{\text{Pl}}}$ and the Earth thin-shell factor from Eq. (2), the AIS guardrail probes the same χ that enters μ_0^{lin} via Eq. (21) below, ensuring a common parameter across cosmology and local tests.

TABLE VII. Quantitative systematics targets enabling the improvements in Table V. Allan deviation σ_y is shown at the indicated averaging times. The uniform tightening factors we adopt here (e.g., $\times 2$ for AU-scale Yukawa limits or $\times (3-10)$ for clock-based ULDM couplings) apply to the quantitative targets listed for the dominant noise terms (cf. Sec. III).

Observable	Dominant term	Quantitative target
PPN γ (radio)	Coronal group delay $\propto f^{-2}$	Dual-frequency Ka/X calibration; residual group delay ≤ 0.1 ns for $b \geq 5 R_\odot$; long dwells (10 d); accelerometry/thermal modeling
PPN γ (optical)	Coronal group delay $\propto f^{-2}$	Optical vs. X: $(f_X/f_{\text{opt}})^2 \simeq 1.8 \times 10^{-9}$; vs. Ka: $(f_{\text{Ka}}/f_{\text{opt}})^2 \simeq 2.6 \times 10^{-8}$. Target: $\geq 5 \times 10^8$ (vs. X) and $\geq 4 \times 10^7$ (vs. Ka) raw reduction; add dual-freq/model margin.
PPN γ, β (global)	Non-grav. accel. modeling	$\lesssim 10^{-11} \text{ m s}^{-2}$ bias over 10-day dwell
\dot{G}/G (LLR)	Normal-point precision	10–30 μm with high-power LLR operations and next-gen CCRs
Yukawa $\alpha_Y(\lambda)$	Asteroid masses/SRP/recoil	Updated catalogs + multi-year DSN arcs
ULDM (clocks)	Link/cavity noise over t_c	Allan deviation $\sigma_y \lesssim 10^{-18}$ at 10^5 – 10^6 s
EEP (AIS)	Differential phase stability	Supports $\eta \sim 10^{-16}$ – 10^{-17} over mission times (via long T , dual-species, and high common-mode rejection)

Writing the differential sensitivity in terms of clock/interferometer coefficients, $\Delta K \equiv \sum_i \Delta K_i d_i$ (cf. Sec. III E and Eq. (18)), Eq. (20) gives

$$\eta(A, B) \simeq 2 \chi_\oplus [\min(1, 3\Delta R_\oplus/R_\oplus)] \Delta K_{\text{eff}},$$

where ΔK_{eff} packages the relevant species coefficients and dark-sector couplings. This makes forecasts transparent: for a target η and a chosen pair (e.g., Rb/K or Sr/Rb), one trades a measured (or design) ΔK_{eff} and the Earth thin-shell factor from (2)–(4) for χ_\oplus , in the same χ that controls μ_0^{lin} via (21). For representative $\Delta K_{\text{eff}} = \mathcal{O}(10^{-1}-1)$ and mission parameters in Tables VI–VII, $\eta \sim 10^{-16}$ – 10^{-17} maps to $|\chi_\oplus| \lesssim 10^{-16}$ – $10^{-17}/\Delta K_{\text{eff}}$ modulo the screening factor, providing a guardrail complementary to Fig. 2.

Beyond static EEP tests, AIS can probe time-dependent signals from ultralight dark matter (ULDM): differential phases oscillate at m_ϕ through species-dependent K_i and d_i (cf. Sec. III E), providing an orthogonal handle to clock networks and extending baselines with space links [44, 48, 49].

A complementary, explicitly DE-driven option is a *tetrahedral* four-spacecraft constellation that measures the trace of the scalar force-gradient tensor in interplanetary space, directly targeting Galileon/Vainshtein phenomenology while rejecting Newtonian backgrounds [50]. While not a traditional single-baseline AI, this DE-focused geometry can incorporate cold-atom accelerometers/gradiometers and fits our decision rule in Sec. V when a specified model predicts a detectable local signature.

IV. COSMOLOGICAL PROBES: DESI, EUCLID, AND COMPLEMENTARITY

A. DESI

The Dark Energy Spectroscopic Instrument (DESI) first data release (DR1) delivers baryon acoustic oscillation (BAO) distance measurements with sub-percent precision across $0.1 < z < 4.2$, using bright galaxy, luminous red galaxy, emission-line galaxy, quasar, and Lyman- α tracers. BAO constraints on the transverse and radial distance combinations, $D_M(z)/r_d$ and $D_H(z)/r_d$, tighten the late-time expansion history; when combined with the cosmic microwave background (CMB) and Big-Bang nucleosynthesis (BBN) priors, extended models show a mild preference for $w_0 > -1$ and $w_a < 0$, while Λ CDM remains statistically viable [12–14].

Beyond BAO, DESI’s full-shape (FS) analysis of the power spectrum, including redshift-space distortions (RSD), jointly constrains geometry and growth⁶. In the flat Λ CDM model, DESI (FS+BAO) with a BBN prior measures $\Omega_m = 0.2962 \pm 0.0095$ and $\sigma_8 = 0.842 \pm 0.034$, while adding CMB data sharpens these to $\Omega_m = 0.3056 \pm 0.0049$ and $\sigma_8 = 0.8121 \pm 0.0053$; inclusion of external clustering+lensing (DES Y3) yields a 0.4% determination of the Hubble parameter, $H_0 = (68.40 \pm 0.27) \text{ km s}^{-1} \text{ Mpc}^{-1}$ [14]. In models with time-varying dark-energy equation of state, DESI (FS+BAO) combined with CMB and supernovae retains the DR1 BAO preference for $w_0 > -1$, $w_a < 0$ at similar significance [14].

⁶ Here BAO denotes baryon acoustic oscillation; FS denotes full-shape; RSD denotes redshift-space distortions; CMB denotes cosmic microwave background; BBN denotes Big-Bang nucleosynthesis; MG denotes modified gravity; GR denotes General Relativity.

DESI also reports constraints on phenomenological modified-gravity (MG) functions that rescale the Poisson equation and lensing, commonly summarized by μ_0 and Σ_0 at $z = 0$. DESI data alone measure $\mu_0 = 0.11^{+0.45}_{-0.54}$; DESI+CMB+DES Y3 give $\mu_0 = 0.04 \pm 0.22$ and $\Sigma_0 = 0.044 \pm 0.047$, consistent with general relativity (GR) [14]. The same analysis places an upper limit on the summed neutrino mass of $\sum m_\nu < 0.071 \text{ eV}$ (95% CL) [14].

B. Euclid

The European Space Agency’s *Euclid* mission Quick Data Release 1 (Q1; March 2025) provides end-to-end validated imaging and spectroscopy over three deep fields totaling $\simeq 63 \text{ deg}^2$, with source catalogs that demonstrate survey-quality photometry, morphology, and point-spread function control across the VIS and NISP instruments⁷ [16, 51]. The Q1 products include tens of millions of galaxy detections (order 10^7) spanning look-back times to $\sim 10.5 \text{ Gyr}$, and early catalogs of strong-lensing systems and clusters that preview the science yield as area accumulates [16, 51]. As the wide survey grows toward the $\gtrsim 15,000 \text{ deg}^2$ goal, cosmology-grade weak-lensing shear and clustering data products will enable precision tests of gravitational slip $\eta \equiv \Phi/\Psi$, scale-dependent growth $f\sigma_8(k, z)$, and consistency with $\Lambda\text{CDM}+\text{GR}$ at the sub-percent level in the two-point statistics [16].

C. Complementarity and cross-checks

Cosmological surveys probe the large-scale, low-potential regime where many modified-gravity or dark-energy scenarios imprint their primary signatures in the expansion history $w(z)$ and in growth/deflection observables summarized by $\mu(z, k)$ and $\Sigma(z, k)$ (cf. Sec. IV). By contrast, Solar-System experiments probe the high-potential, screened regime and impose model-independent guardrails through the Einstein equivalence principle (EEP), the parameterized post-Newtonian (PPN) coefficients γ and β , and bounds on \dot{G}/G (Sec. III). The multimessenger bound on the gravitational-wave speed, $|c_{\text{T}}/c - 1| \lesssim 10^{-15}$, links the two regimes by excluding broad classes of low-energy modifications or forcing them close to General Relativity on both cosmological and local scales [8, 9].

A quantitative workflow is two-stage. First, DESI BAO+FS and *Euclid* weak-lensing and clustering determine the posterior in the cosmology-level parameter space $\{w(z), \mu(z, k), \Sigma(z, k)\}$; in a scalar-tensor embedding this corresponds to restrictions on the effective $\{V(\phi), A(\phi)\}$ subject to the c_{T} constraint (Sec. I). Second, given these posteriors, one maps to predicted local residuals using the screening relations of Sec. II: for chameleon-like models via the thin-shell expressions [(2)–(7), (22)–(24)] and for Vainshtein-like models via the Vainshtein radius and residual scalings (10)–(11). This yields concrete targets for Solar-System tests such as $|\gamma - 1|$ at solar conjunction, $\beta - 1$ in ephemerides, and environment-dependent EEP/clock effects at levels set by the relevant potentials Φ_N (7). A null detection at the forecast sensitivity prunes the cosmologically allowed model subspace; a detection triggers a joint re-fit across regimes with the same microphysical parameters. In our universal conformal benchmark with negligible anisotropic stress on linear scales, the metric potentials remain nearly equal ($\Phi \simeq \Psi$), so the lensing response $\Sigma(z, k)$ tracks the clustering response $\mu(z, k)$ up to $\mathcal{O}(1)$ factors. Operationally, we therefore take $\mu_{\text{lin},0}$ as the primary cosmology→local bridge parameter and quote Σ_0 only for cross-checks.

1. Illustrative mapping (worked example)

Consider a conformally coupled scalar with $A(\phi) = \exp(\chi\phi/M_{\text{Pl}})$ and a chameleon-like runaway potential, e.g. $V(\phi) = \Lambda^{4+n}\phi^{-n}$ with $n > 0$, so that thin-shell screening applies [Eqs. (2)–(7)]. With these explicit choices, linear growth is enhanced by $\mu(z, k) \simeq 1 + 2\chi^2$ in the unscreened regime. Define $\mu_0^{\text{lin}} \equiv \mu(z=0, k \sim 0.1 \text{ h Mpc}^{-1}) - 1$. Suppose DESI+Euclid posteriors favored $\mu_0^{\text{lin}} = 0.10 \pm 0.05$ at $z \simeq 0$ (illustrative). Interpreting this in the conformal scalar model yields

$$\chi \simeq \sqrt{\frac{\mu_0^{\text{lin}}}{2}} \approx 0.224, \quad (21)$$

indicating an $\mathcal{O}(10\%)$ unscreened enhancement of linear clustering. As noted in Sec. II, we adopt $k \simeq 0.1 \text{ h Mpc}^{-1}$ for μ_0^{lin} ; forecasts inherit only a mild k -dependence from $\mu(z, k)$. For context, panels (b)–(c) of Fig. 1 illustrate how

⁷ Here VIS denotes the visible imager; NISP denotes the near-infrared spectrometer and photometer.

a given $\mu_{\text{lin},0}$ maps into the required Sun thin-shell (via Eqs. (21)–(24)) and the corresponding conjunction targets. Note that in Sec. IV, the cosmology→local map assumes a *screened Sun* (thin shell), so that (2) and (22) apply; unscreened interpretations of a nonzero μ_0^{lin} would instead be pruned directly by solar-conjunction bounds on γ .

Locally, the Sun must be screened to respect solar-conjunction bounds on the PPN parameter γ . For a chameleon-like thin shell [Eq. (2)], the effective scalar charge of a screened body scales as $\alpha_\odot \simeq 3\chi (\Delta R/R)$, so for $|\alpha_\odot| \ll 1$ the leading metric deviation near the Sun can be estimated as

$$|\gamma - 1| \simeq 2\alpha_\odot^2 \simeq 18\chi^2 \left(\frac{\Delta R}{R}\right)^2. \quad (22)$$

The coefficient in $|\gamma - 1| \simeq 2\alpha_\odot^2$ is model-normalization dependent; with $\alpha_\odot = 3\chi \Delta R/R$ our normalization yields (22). Other conventions map by $\mathcal{O}(1)$ factors and do not affect the forecasts here. Demanding that the next-generation solar-conjunction analyses reach and do not detect $|\gamma - 1| \lesssim 5 \times 10^{-6}$ implies

$$\frac{\Delta R}{R} \lesssim \frac{1}{3\chi} \sqrt{\frac{|\gamma - 1|}{2}} \approx 2.36 \times 10^{-3} \quad (\chi \simeq 0.224, |\gamma - 1| = 5 \times 10^{-6}). \quad (23)$$

Using the thin-shell relation [Eq. (2)] with the Sun’s surface potential $\Phi_{N\odot} \simeq 2.12 \times 10^{-6}$ [Eq. (7), see Table 1] then bounds the allowed field excursion across the shell:

$$|\phi_\infty - \phi_c| \lesssim 6\chi M_{\text{Pl}} \Phi_{N\odot} \frac{\Delta R}{R} \approx 6.7 \times 10^{-9} M_{\text{Pl}}. \quad (24)$$

Eqs. (23)–(24) quantify how a modest, cosmology-level deviation ($\mu_0^{\text{lin}} \sim 0.1$) maps to a concrete Solar-System requirement: a Sun thin-shell factor at the 10^{-3} level and a correspondingly small environmental field contrast. Failure to satisfy these would produce a detectable $|\gamma - 1|$ signal; conversely, a null solar-conjunction result at the 10^{-6} level would exclude the unscreened interpretation of $\mu_0^{\text{lin}} \sim 0.1$ unless the chameleon parameters enforce $\Delta R/R \lesssim 10^{-3}$.

Fig. 2 visualizes (23) by showing the required solar thin shell $\Delta R/R$ as a function of the cosmology-level response $\mu_{\text{lin},0}$ for two null-test targets on $|\gamma - 1|$. For a given cosmology-level excess $\mu_{\text{lin},0}$, a null solar-conjunction result at sensitivity $|\gamma - 1|_{\text{max}}$ implies a maximum allowed Sun thin-shell fraction $\Delta R/R$ via (23) with curves labeled by $|\gamma - 1|_{\text{max}} = 5 \times 10^{-6}$ and 1×10^{-6} . For the working example $\mu_{\text{lin},0} \simeq 0.10$, the 5×10^{-6} goal requires $\Delta R/R \lesssim 2.4 \times 10^{-3}$ (Eqs. (21)–(24)).

For comparison, in a Vainshtein-screened model (e.g., a cubic Galileon) with Solar Vainshtein radius $r_{V\odot}$ given by (10) and the numerical values in (11), the residual fractional modification inside the Vainshtein region scales as $(r/r_V)^{3/2}$ for the force-law correction [5, 52]. At $r = 1 \text{ AU}$ and $r_{V\odot} \simeq 1.2 \times 10^2 \text{ pc}$, this yields $\delta F/F \sim (1 \text{ AU}/100 \text{ pc})^{3/2} \sim 10^{-11}$, far below current and near-term sensitivity, thereby illustrating why Solar-System constraints are naturally weak for Vainshtein screening even if cosmology shows percent-level deviations. (For definiteness, a cubic Galileon sector with $\mathcal{L}_3 \sim (\partial\phi)^2 \square\phi/\Lambda^3$ provides the derivative self-interaction.)

Combining Eqs. (3)–(4) with Eq. (23) and the screened limit $\phi_c \ll \phi_\infty$ gives

$$\phi_\star(\rho_\infty) \leq M_{\text{Pl}} \Phi_{N\odot} \sqrt{2|\gamma - 1|_{\text{max}}}, \quad (25)$$

so that

$$\Lambda^{4+n} \leq \frac{\chi \rho_\infty}{n M_{\text{Pl}}} \left[M_{\text{Pl}} \Phi_{N\odot} \sqrt{2|\gamma - 1|_{\text{max}}} \right]^{n+1}. \quad (26)$$

Note that with $[\rho] = \text{energy density}$ and $[\Lambda] = \text{energy}$, (26) preserves $[\Lambda^{4+n}]$ on both sides; the factor n^{-1} follows from $V'(\phi_\star) + \rho A'(\phi_\star) = 0$ for $V(\phi) = \Lambda^{4+n} \phi^{-n}$. Eqs. (25)–(26) recover the $\rho_\infty^{-1/(n+1)}$ thin-shell scaling when eliminating Λ against a cosmology-level normalization, as shown explicitly in Appendix D.

Given μ_0^{lin} (hence $\chi \simeq \sqrt{\mu_0^{\text{lin}}/2}$ from (21)) and an adopted ambient density ρ_∞ appropriate to the near-Sun environment, (26) translates the conjunction sensitivity directly into a bound on Λ for each n . For the illustrative case $\mu_0^{\text{lin}} = 0.10 \Rightarrow \chi \simeq 0.224$ and $|\gamma - 1|_{\text{max}} = 5 \times 10^{-6}$, (26) gives $\Lambda^{4+n} \leq (\chi \rho_\infty / n M_{\text{Pl}}) [M_{\text{Pl}} \Phi_{N\odot} \sqrt{10^{-5}}]^{n+1}$. Given μ_0^{lin} we infer $\chi \simeq \sqrt{\mu_0^{\text{lin}}/2}$ (21). Together with (3)–(4) and the Solar-System bounds (23), (25), this makes the (n, Λ) dependence of the forecasts explicit (see also (26)).

V. WHAT SHOULD A SOLAR-SYSTEM PROGRAM LOOK LIKE?

Fig. 1 assembles the measurement landscape: (a) dispersion scaling, (b) conjunction γ reach vs. b/R_\odot , (c) the implied thin-shell bound, and (d) clock sensitivity to d_e vs. m_ϕ under current vs. advanced links. Using the thin-shell relation in (23), Fig. 2 shows the resulting $\Delta R/R$ versus $\mu_{\text{lin},0}$ for two choices of $|\gamma - 1|_{\text{max}}$.

TABLE VIII. Illustrative mapping from cosmology-level posteriors to Solar-System residual targets. Numbers are indicative to show usage of Eqs. (2)–(11), (21)–(24).

Model	Cosmology posterior	Mapping param	Local target(s)	Notes
Conformal scalar	$\mu_0^{\text{lin}} = 0.10 \pm 0.05$	$\chi = \sqrt{\mu_0^{\text{lin}}/2} \simeq 0.224$	$ \gamma - 1 \lesssim \text{few} \times 10^{-6}; \Delta R/R \lesssim (1.6\text{--}2.4) \times 10^{-3}$	Eqs. (21)–(24)
Cubic Galileon	Σ_0, μ_0 consistent with GR	$r_{V\odot} \sim 10^2 \text{ pc}$	$\delta F/F(1 \text{ AU}) \sim (r/r_V)^{3/2} \sim 10^{-11}$	Eqs. (10)–(11)
Yukawa tail	$\alpha(\lambda)$ at $\lambda = 10^9\text{--}10^{13} \text{ m}$	$m = \hbar c/\lambda$	$ \alpha_Y \ll 10^{-9}\text{--}10^{-10}$	Sec. III D
ULDM (scalar)	coupling d_i vs. m_ϕ	$t_c \simeq 2\pi/(m_\phi v^2)$	$\delta\nu/\nu \sim K_i d_i \phi_0$; improve $\times(3\text{--}10)$	Sec. III E

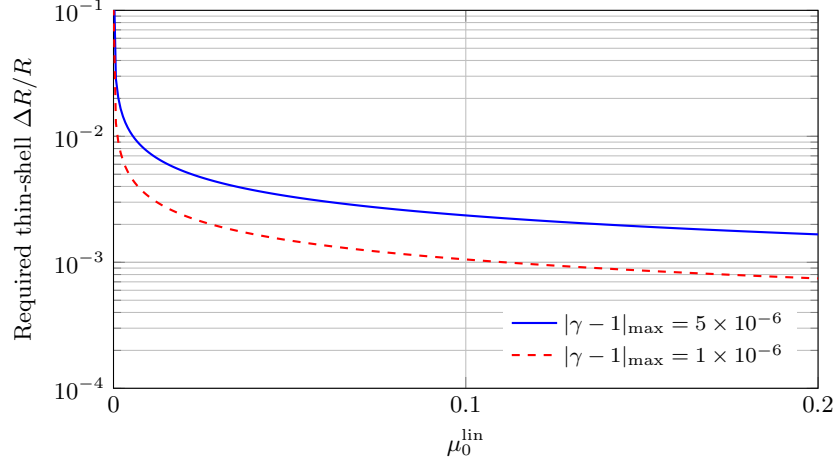


FIG. 2. Thin-shell requirement for the Sun implied by a null detection of solar-conjunction PPN γ at sensitivity $|\gamma - 1|_{\text{max}}$ as a function of the cosmology-level linear response μ_0^{lin} in the conformal scalar benchmark (adopts $k \simeq 0.1 h \text{ Mpc}^{-1}$ for μ_0^{lin} ; see Sec. II.) For $\mu_0^{\text{lin}} \simeq 0.10$, the $|\gamma - 1| \lesssim 5 \times 10^{-6}$ target implies $\Delta R/R \lesssim 2.4 \times 10^{-3}$ [Eqs. (21)–(24)]. (See Appendix C.)

Based on the analysis above, we recommend a targeted, cost-effective portfolio that rides on planned space assets and existing ground infrastructure.

1. *Solar-conjunction radio science for γ and β* : Implementation: multi-frequency Ka/X links with BepiColombo/MORE and future conjunction opportunities, improved coronal-plasma calibration (dual-frequency group-delay and Faraday-rotation constraints with contemporaneous solar data), optimized low-impact-parameter arcs ($b/R_\odot \simeq 3\text{--}5$) and long dwell times ($\gtrsim 10$ days) (see Fig. 2). Quantitative target: $|\gamma - 1| \lesssim \text{few} \times 10^{-6}$ per conjunction; comparable sensitivity to $\beta - 1$ from global ephemeris fits. Dominant systematics: coronal turbulence and dispersion modeling, spacecraft non-gravitational accelerations, tropospheric delay calibration [24, 25].
2. *Sustained millimeter-class LLR*: Implementation: next-generation corner-cube retroreflectors with reduced thermal gradients, higher link budgets (kW-class lasers, larger apertures), improved station timing/metrology, and consistent global analysis with modern planetary ephemerides. Quantitative target: $|\dot{G}/G| \lesssim \text{few} \times 10^{-14} \text{ yr}^{-1}$; factor 3–7 \times tightening of SEP (Nordtvedt) constraints relative to current solutions. Dominant systematics: station geometry and thermal control, retroreflector thermal lensing, model degeneracies with tidal parameters [31, 32, 53].
3. *Global optical clock links (ground + space)*: Implementation: long-baseline optical time/frequency transfer (ACES and follow-on optical links), multi-species comparisons to decorrelate sensitivity coefficients K_i , and campaign lengths exceeding coherence times for the targeted ultralight-mass window. Quantitative target: improvement by a factor 3–10 in scalar-coupling bounds across $m_\phi \sim 10^{-24}\text{--}10^{-15} \text{ eV}$; fractional stability at $10^{-18}\text{--}10^{-19}$ over $10^5\text{--}10^6 \text{ s}$ typical integration. Dominant systematics: link noise and cycle slips, environmental couplings (temperature, magnetic fields), long-term drift of reference cavities [40–43].
4. *Ephemerides and small-force systematics*: Implementation: reprocess Deep Space Network tracking with updated media calibrations, extend multi-year arcs, refine asteroid catalogs and nongravitational-force models (thermal recoil, solar radiation pressure), and perform joint fits with improved solar-corona priors. Quantitative

target: factor ~ 2 tightening of AU-scale Yukawa strength limits $|\alpha(\lambda)|$ across $\lambda \sim 10^9\text{--}10^{13}$ m and of smooth Solar-System dark-matter density bounds (e.g., at Saturn's orbit from $\sim 1 \times 10^{-20}$ to $\sim 5 \times 10^{-21}$ g cm $^{-3}$). Dominant systematics: asteroid-mass uncertainties, spacecraft thermal systematics, solar-plasma residuals in inner-planet ranges [31, 35].

5. *Space atom interferometer (AIS) for EEP*: Implementation: drag-free spacecraft, dual-/multi-species interferometers with long T and common-mode rejection. Quantitative target: $\eta \sim 10^{-16}\text{--}10^{-17}$ under realistic T and vibration budgets; sensitivity to ULDM-induced, species-dependent modulations across $m_\phi \sim 10^{-24}\text{--}10^{-15}$ eV complementary to clock networks. Dominant systematics: gravity gradients and magnetic backgrounds; addressed by gradient compensation, magnetic shielding, and drag-free control. *Notes*: Constellation options (e.g., tetrahedral trace measurements) provide an explicitly DE-driven path targeting Galileon/Vainshtein sectors [20, 21, 50].

Below is the systematic risk summary for a near-term program:

- *Near-Sun optical links*: Plasma group delay scales as f^{-2} ; for $b \lesssim 5R_\odot$ stray light and thermal drifts dominate. *Require* terminal pointing jitter $\leq 1 \mu\text{rad}_{\text{RMS}}$ (0.1–10 Hz), pupil temperature gradients $\leq 0.5 \text{ K}_{\text{RMS}}$ over $10^2\text{--}10^3$ s, and in-band stray-light suppression $\geq 10^7$ at the detector. *Mitigate* with apodized baffling, narrowband filtering/FOV control, and active thermal regulation of the optical head.
- *LLR micro-metrology*: CCR thermal lensing and station timing chains can saturate gains. *Require* CCR $\Delta T \leq 0.1 \text{ K}$ over 10^3 s, event-timer jitter $\leq 3 \text{ ps RMS}$, verified two-way time transfer $\leq 10 \text{ ps}$, and station reference $\sigma_y(100\text{--}1000 \text{ s}) \leq 3 \times 10^{-15}$. *Mitigate* with IR wavelengths and single-CCR designs, timer cross-calibration, and redundant calibration passes.
- *Ephemerides*: Asteroid mass priors and solar-plasma residuals can bias AU-scale $\alpha(\lambda)$. *Require* inclusion of ≥ 300 main-belt asteroids with $\sigma_M/M \leq 20\%$, and Ka-band corona calibration with residual group delay $\leq 0.1 \text{ ns}$ for $b \geq 5R_\odot$. *Mitigate* via joint fits with contemporaneous solar-wind/TEC data and periodic catalog updates/reweighting of conjunction windows.
- *Clocks/links*: Over the expected coherence time t_c , link and cavity noise must be subdominant. *Require* end-to-end instability $\sigma_y(\tau=t_c) \leq 3 \times 10^{-16}$, cycle-slip probability $< 10^{-6}$ per t_c , optical-comb integrated phase noise (1 Hz–1 kHz) $\leq 0.3 \text{ rad}$, and multi-species comparisons with $|\Delta K_i| \geq 0.1$ to decorrelate couplings. *Mitigate* via dual independent links, real-time slip detection/repair, and alternating species schedules.
- *Precision gradiometry*: Formation-keeping and scale-factor drift can masquerade as beyond-PPN signals. *Require* $\leq 10 \text{ pm}/\sqrt{\text{Hz}}$ inter-satellite laser metrology and $\leq 10 \text{ nrad}/\sqrt{\text{Hz}}$ attitude jitter (1–100 mHz), baseline knowledge $\leq 1 \text{ mm}$ (10–100 km), and bias stability $\leq 1 \times 10^{-12} \text{ m s}^{-2}$ over 10^4 s . *Mitigate* with sign-reversal geometries, calibration slews, and thermal scale-factor tracking.
- *Space-based atom interferometry (AIS)*: Vibration, wavefront, and B -gradient systematics dominate for long- T . *Require* drag-free $\leq 3 \times 10^{-15} \text{ m s}^{-2}/\sqrt{\text{Hz}}$ (0.1–10 mHz), magnetic-field gradients $\leq 1 \text{ nT m}^{-1}$, Raman/Bragg phase noise $\leq 1 \text{ mrad}/\sqrt{\text{Hz}}$, and common-mode rejection $\geq 120 \text{ dB}$ to reach $\eta \approx 10^{-16}\text{--}10^{-17}$ with $T \geq 5\text{--}10 \text{ s}$. *Mitigate* with active vibration cancellation, magnetic shielding/trim coils, wavefront sensing, and continuous slip detection.

Further improvements are possible: Optical links enable PPN tests with substantially reduced coronal plasma noise (dispersion $\propto f^{-2}$), offering $\sim 10^8\text{--}10^9$ lower group-delay systematics than X/Ka at $f \sim 2 \times 10^{14} \text{ Hz}$ [23]. Interplanetary laser ranging (ILR) has already demonstrated sub-ns timing over tens of millions of km with asynchronous laser transponders, validating Shapiro-delay-grade timing on optical carriers [54]. Recent deep-space optical communications (DSOC) links have shown robust high-rate operation at $\sim 0.2\text{--}1.5 \text{ AU}$, indicating operational readiness of narrow-beam, high-SNR optical terminals for precise time/frequency transfer [55]. For LLR, high-power 1064 nm systems and differential LLR (dLLR) [32] with next-generation CCRs [53] can drive normal-point precision toward the $\sim 30 \mu\text{m}$ regime, tightening constraints on \dot{G}/G and SEP (via the Nordtvedt parameter) and improving β through global fits [56, 57]. Concept studies of optical deflection/near-Sun astrometry (e.g., LATOR) further indicate potential improvements in γ sensitivity by orders of magnitude if stray-light and thermal-control issues are addressed [58].

Decision rule for dedicated Solar-System missions: authorize only when a specified microphysical model or well-defined model class, with explicit $\{V(\phi), A(\phi)\}$ (or the relevant dark-matter coupling), predicts at least one local signature—such as a target for $\gamma - 1$, $\beta - 1$, \dot{G}/G , a Yukawa amplitude $\alpha(\lambda)$, or a clock modulation—exceeding a credible detection threshold given Solar-System potentials. Otherwise, emphasize the piggybacked radio-science, LLR, clock-link, and ephemeris options above as the highest return per cost [24, 25, 31, 32, 35, 40–43]. (Concept

studies also consider multi-arm or tetrahedral geometries to enhance common-mode rejection and gradient control [50].)

VI. CONCLUSIONS

Solar-System experiments are not generic fishing exercises. Under the theoretical priors stated in Sec. I and the screening relations of Sec. II, they are hypothesis-driven tests that (i) enforce universal guardrails any dark-energy or dark-matter model must satisfy, (ii) close unscreened or weakly screened corners of theory space, and (iii) provide genuine discovery windows for ultralight or long-range sectors. The multimessenger bound on the gravitational-wave speed, $|c_T/c - 1| \lesssim 10^{-15}$ [8, 9], further couples cosmological and local regimes, making cross-checks logically tight rather than exploratory.

Our recommended strategy is asymmetric. Cosmology carries the discovery prior for late-time acceleration; DESI and *Euclid* determine $\{w(z), \mu(z, k), \Sigma(z, k)\}$ at percent-level precision in two-point statistics (Sec. IV). The Solar-System program then targets the specific residuals implied by those posteriors, at forecastable levels set by Solar-System potentials Φ_N and by the screening maps in Eqs. (2)–(7), (22)–(24), and (10)–(11). Concretely, the near-term measurement goals in Sec. III and the program elements in Sec. V deliver:

1. $|\gamma - 1| \lesssim \text{few} \times 10^{-6}$ per solar conjunction using Ka/X or optical links with improved coronal calibration (optical strongly suppresses plasma terms); comparable sensitivity to $\beta - 1$ from global fits. Target the $\lesssim 1 \times 10^{-8}$ regime with advanced astrometric and/or optical metrology experiments [58–60].
2. $|\dot{G}/G| \lesssim \text{few} \times 10^{-14} \text{ yr}^{-1}$ and a factor 2–3 tightening of SEP (Nordtvedt) constraints via millimeter-class LLR with next-generation retroreflectors and station upgrades. Expect a factor of 10–50 improvement with the new high-power LLR facilities and new CCRs [32, 53].
3. A factor 3–10 improvement in clock-based limits on ultralight-scalar couplings across $m_\phi \sim 10^{-24} - 10^{-15} \text{ eV}$ using long-baseline ground-space optical links. Tetrahedral spacecraft formations with optical metrology and AIS offer additional factor of 25–50 improvements [50].
4. A factor ~ 2 strengthening of AU-scale Yukawa bounds $|\alpha_Y(\lambda)|$ for $\lambda \sim 10^9 - 10^{13} \text{ m}$, and of smooth Solar-System dark-matter density limits (e.g., at Saturn’s orbit from $\sim 1.1 \times 10^{-20}$ to $\sim 5 \times 10^{-21} \text{ g cm}^{-3}$) through DSN reprocessing and refined ephemerides.
5. Precision EEP: retain MICROSCOPE-level guardrails and target $\eta \sim 10^{-16} - 10^{-17}$ with a drag-free AIS (as a universal test, not a model-blind DE probe).

The cross-regime mapping is numerically tractable. For example, an illustrative cosmology-level excess $\mu_0^{\text{lin}} \simeq 0.10$ at $k \simeq 0.1 h \text{ Mpc}^{-1}$ implies $\chi \simeq 0.224$ for a conformally coupled scalar. Solar-conjunction bounds taking $|\gamma - 1| \lesssim (2 - 5) \times 10^{-6}$ yields $\Delta R/R \lesssim (1.6 - 2.4) \times 10^{-3}$ and $|\phi_\infty - \phi_c| \lesssim (4.3 - 6.7) \times 10^{-9} M_{\text{Pl}}$ [Eqs. (2)–(24)]. A null result at that sensitivity prunes the unscreened interpretation of the cosmological signal; a detection demands a joint re-fit of cosmology and Solar-System data with the same microphysical parameters. In Vainshtein-screened models, by contrast, the residual at 1 AU scales as $(r/r_V)^{3/2} \sim 10^{-11}$ for $r_{V\odot} \sim 10^2 \text{ pc}$, explaining the natural weakness of local tests even when cosmology shows percent-level deviations (Sec. II).

Finally, we emphasize that Solar-System experiments constrain DE and DM in distinct, complementary ways:

- *For DE*, screening in deep Solar potentials typically suppresses predicted local residuals (e.g., $\gamma - 1$, $\beta - 1$, \dot{G}/G) to *at or just below* current sensitivity — often within a factor of ~ 2 –4 of present bounds, with the precise target set by the ambient density ρ_∞ (see (23) and Table III). The role of local tests is therefore (i) to enforce universal null tests (EEP/PPN: γ , β , η_{SEP} , \dot{G}/G) and (ii) to interrogate *targeted, plausibly unscreened* corners that DESI/*Euclid* flag via the theory bridge $V_{\text{eff}}(\phi; \rho) = V(\phi) + \rho A(\phi)$.
- *For DM*, by contrast, Solar-System probes offer *selective discovery reach* with clean systematics and direct parameter-signal maps: long-baseline clock networks and atom interferometers for ultralight fields ($m_\phi \sim 10^{-24} - 10^{-15} \text{ eV}$; coherence-limited searches), high-precision ephemerides for AU-scale Yukawa forces ($\lambda \sim 10^9 - 10^{13} \text{ m}$; $\lambda \equiv \hbar/(m_\phi c)$), and, where metric couplings apply, light-propagation tests (Shapiro delay/deflection) constraining γ .

Thus, dedicated Solar-System missions are warranted when a specified microphysical model with explicit $\{V(\phi), A(\phi)\}$ (or an explicit dark-sector candidate) predicts at least one *local* signature that exceeds credible detection thresholds

after allocating systematic-error budgets — preferably by a factor of a few for margin (cf. Eq. (23), Table III). Otherwise, piggybacked radio/optical links, mm-class LLR, networked clocks/AIs, and ephemeris reprocessing deliver the highest science return per cost (Sec. V).

Intrinsic limitations remain: local tests primarily probe spatial modes near the AU scale ($k \sim \text{AU}^{-1}$); they are systematics-limited (e.g., coronal plasma for radio, strongly mitigated by optical links; station geometry/thermal effects for LLR; asteroid masses and non-gravitational forces in ephemerides) and require an explicit theory map from cosmological posteriors to local residuals.

Within these bounds, Solar-System experiments act as precision discriminants: they either reveal residual new physics consistent with cosmological hints in the targeted sectors above, or they excise model families that would otherwise remain viable from cosmology alone.

ACKNOWLEDGMENTS

The author expresses gratitude to Curt J. Cutler, Jason D. Rhodes and Eric M. Huff of JPL who provided valuable comments, encouragement, and stimulating discussions while this document was in preparation. The work described here was carried out at the Jet Propulsion Laboratory, California Institute of Technology, Pasadena, California, under a contract with the National Aeronautics and Space Administration.

-
- [1] J. Khoury and A. Weltman, Chameleon Fields, [Phys. Rev. D](#) **69**, 044026 (2004).
 - [2] J. Khoury and A. Weltman, Chameleon Fields: Awaiting Surprises for Tests of Gravity in Space, [Phys. Rev. Lett.](#) **93**, 171104 (2004).
 - [3] K. Hinterbichler and J. Khoury, Symmetron Fields: Screening Long-Range Forces Through Local Symmetry Restoration, [Phys. Rev. Lett.](#) **104**, 231301 (2010).
 - [4] C. Burrage and J. Sakstein, Tests of Chameleon Gravity, [Living Reviews in Relativity](#) **21**, 1 (2018).
 - [5] K. Koyama, Cosmological Tests of Modified Gravity, [Reports on Progress in Physics](#) **79**, 046902 (2016).
 - [6] LIGO Scientific Collaboration and Virgo Collaboration, GW170817: Observation of gravitational waves from a binary neutron star inspiral, [Phys. Rev. Lett.](#) **119**, 161101 (2017).
 - [7] LIGO Scientific Collaboration, Virgo Collaboration, *et al.*, Multi-messenger observations of a binary neutron star merger, [Astrophys. J. Lett.](#) **848**, L12 (2017).
 - [8] T. Baker, E. Bellini, P. G. Ferreira, M. Lagos, J. Noller, and I. Sawicki, Strong Constraints on Cosmological Gravity from GW170817 and GRB 170817A, [Phys. Rev. Lett.](#) **119**, 251301 (2017).
 - [9] P. Creminelli and F. Vernizzi, Dark Energy after GW170817 and GRB170817A, [Phys. Rev. Lett.](#) **119**, 251302 (2017).
 - [10] J. M. Ezquiaga and M. Zumalacárregui, Dark Energy after GW170817: Dead Ends and the Road Ahead, [Phys. Rev. Lett.](#) **119**, 251304 (2017).
 - [11] A. Adams, N. Arkani-Hamed, S. Dubovsky, A. Nicolis, and R. Rattazzi, Causality, Analyticity and an IR Obstruction to UV Completion, [JHEP](#) **2006** (10), 014.
 - [12] DESI Collaboration, The DESI Experiment Part I: Science, Targeting, and Survey Design, arXiv e-prints (2016), [arXiv:1611.00036 \[astro-ph.IM\]](#).
 - [13] DESI Collaboration, DESI 2024 VI: Cosmological Constraints from the Measurements of Baryon Acoustic Oscillations (BAO), [JCAP](#) **2025** (02), 021.
 - [14] DESI Collaboration, DESI 2024 VII: Cosmological Constraints from the Full-Shape Modeling of Clustering Measurements, [JCAP](#) **2025** (07), 028.
 - [15] Euclid Collaboration, A. Blanchard, S. Camera, C. Carbone, V. F. Cardone, S. Casas, S. Clesse, and *et al.*, Euclid preparation. VII. Forecast validation for Euclid cosmological probes, [Astronomy & Astrophysics](#) **642**, A191 (2020).
 - [16] Euclid Collaboration, H. Aussel, I. Tereno, M. Schirmer, G. Alguero, B. Altieri, E. Balbinot, T. de Boer, and *et al.*, Euclid Quick Data Release (Q1) – Data release overview (2025), [arXiv:2503.15302 \[astro-ph.GA\]](#).
 - [17] S. G. Turyshev, U. E. Israelsson, M. Shao, N. Yu, A. Kusenko, E. L. Wright, C. W. F. Everitt, M. Kasevich, J. A. Lipa, J. C. Mester, R. D. Reasenberg, R. L. Walsworth, N. Ashby, H. Gould, and H. J. Paik, Space-Based Research in Fundamental Physics and Quantum Technologies, [Int. J. Mod. Phys. D](#) **16**, 1879 (2007), [arXiv:0711.0150 \[gr-qc\]](#).
 - [18] S. G. Turyshev, Experimental tests of general relativity: recent progress and future directions, [Physics Uspekhi](#) **52**, 1 (2009), [arXiv:0809.3730 \[gr-qc\]](#).
 - [19] P. Touboul *et al.*, Space test of the Equivalence Principle: MICROSCOPE final results, [Phys. Rev. Lett.](#) **129**, 121102 (2022).
 - [20] B. Battelier *et al.*, Exploring the Foundations of the Universe with Space-Based Atom Interferometry, [Experimental Astronomy](#) **51**, 1695 (2021).
 - [21] N. Gaaloul, H. Ahlers, L. Badurina, A. Bassi, B. Battelier, Q. Beaufiles, and *et al.*, STE-QUEST – Space Time Explorer and QUantum Equivalence principle Space Test: The 2022 medium-class mission concept (2022), [arXiv:2211.15412 \[physics.space-ph\]](#).

- [22] C. M. Will, The Confrontation Between General Relativity and Experiment, [Living Reviews in Relativity](#) **17**, 4 (2014), and updates.
- [23] B. Bertotti, L. Iess, and P. Tortora, A test of general relativity using radio links with the Cassini spacecraft, [Nature](#) **425**, 374 (2003).
- [24] L. Iess and et al., Gravity, Geodesy and Fundamental Physics with BepiColombo's MORE Investigation, [Space Sci. Rev.](#) **217**, 10.1007/s11214-021-00800-3 (2021).
- [25] I. di Stefano, P. Cappuccio, and L. Iess, The BepiColombo solar conjunction experiments revisited, [CQG](#) **38**, 055002 (2021).
- [26] NASA Jet Propulsion Laboratory, NASA's Deep Space Optical Comm Demo Sends, Receives First Data, <https://www.jpl.nasa.gov/news/nasas-deep-space-optical-comm-demo-sends-receives-first-data/> (2023), news release.
- [27] NASA Jet Propulsion Laboratory, NASA's Laser Comms Demo Makes Deep Space Record, Completes First Phase, <https://www.jpl.nasa.gov/news/nasas-laser-comms-demo-makes-deep-space-record-completes-first-phase/> (2024), news release.
- [28] NASA, Deep Space Optical Communications (DSOC), <https://www.nasa.gov/mission/deep-space-optical-communications-dsoc/> (2025), mission page; page last updated 2025-02-28.
- [29] J. G. Williams, S. G. Turyshev, and D. H. Boggs, Progress in Lunar Laser Ranging Tests of Relativistic Gravity, [Phys. Rev. Lett.](#) **93**, 261101 (2004).
- [30] E. V. Pitjeva, N. P. Pitjev, D. A. Pavlov, and C. C. Turygin, Estimates of the change rate of solar mass and gravitational constant based on the dynamics of the Solar System, [Astron. Astrophys.](#) **647**, A141 (2021).
- [31] A. Fienga and O. Minazzoli, Testing theories of gravity with planetary ephemerides, [Living Reviews in Relativity](#) **27**, 1 (2024).
- [32] S. G. Turyshev, Lunar laser ranging with high-power continuous-wave lasers, [Phys. Rev. Applied](#) **23**, 064066 (2025), [arXiv:2502.02796 \[astro-ph.IM\]](#).
- [33] L. Biskupek, J. Müller, and J.-M. Torre, Benefit of New High-Precision LLR Data for the Determination of Relativistic Parameters, [Universe](#) **7**, 34 (2021).
- [34] C. Talmadge, J.-P. Berthias, R. W. Hellings, and E. M. Standish, Model-Independent Constraints on Possible Modifications of Newtonian Gravity, [Phys. Rev. Lett.](#) **61**, 1159 (1988).
- [35] E. V. Pitjeva and N. P. Pitjev, Relativistic effects and dark matter in the Solar system from observations of planets and spacecraft, [Mon. Not. R. Astron. Soc.](#) **432**, 3431 (2013).
- [36] N. P. Pitjev and E. V. Pitjeva, Constraints on dark matter in the solar system, [Astronomy Letters](#) **39**, 141 (2013).
- [37] K. Van Tilburg, N. Leefer, L. Bougas, and D. Budker, Search for Ultralight Scalar Dark Matter with Atomic Spectroscopy, [Phys. Rev. Lett.](#) **115**, 011802 (2015).
- [38] Y. V. Stadnik and V. V. Flambaum, Searching for Dark Matter and Variation of Fundamental Constants with Laser and Maser Interferometry, [Phys. Rev. Lett.](#) **114**, 161301 (2015).
- [39] A. Arvanitaki, J. Huang, and K. Van Tilburg, Searching for Dilaton Dark Matter with Atomic Clocks, [Phys. Rev. D](#) **91**, 015015 (2015).
- [40] A. Hees *et al.*, Searching for an oscillating massive scalar field as a dark matter candidate using atomic hyperfine frequency comparisons, [Phys. Rev. Lett.](#) **117**, 061301 (2016).
- [41] P. Wcisło *et al.*, New bounds on dark matter coupling from a global network of optical atomic clocks, [Science Advances](#) **4**, eaau4869 (2018).
- [42] L. Cacciapuoti and C. Salomon, Space clocks and fundamental tests: The ACES experiment, [Eur. Phys. J. Special Topics](#) **172**, 57 (2009).
- [43] P. Delva, H. Denker, G. Lion, P.-E. Pottie, and et al., Test of Special Relativity Using a Fiber Network of Optical Clocks, [Phys. Rev. Lett.](#) **118**, 221102 (2017).
- [44] G. M. Tino and et al., SAGE: A Proposal for a Space Atomic Gravity Explorer, [Eur. Phys. J. D](#) **73**, 228 (2019).
- [45] L. Badurina *et al.*, AION: An atom interferometer observatory and network, [JCAP](#) (5), 011, 1911.11755.
- [46] Y. Abou El-Neaj *et al.*, AEDGE: Atomic Experiment for Dark Matter and Gravity Exploration in Space, [EPJ Quantum Technology](#) **7**, 6 (2020).
- [47] J. Williams, S.-w. Chiow, N. Yu, and H. Müller, Quantum test of the equivalence principle and space-time aboard the International Space Station, [New J. Phys.](#) **18**, 025018 (2016).
- [48] L. Badurina and et al., Prospective Sensitivities of Atom Interferometers to Gravitational Waves and Ultralight Dark Matter, [JHEP](#) (05), 011.
- [49] M. Abe and et al., Matter-wave Atomic Gradiometer Interferometric Sensor (MAGIS-100) (2021), concept and science case for 100 m AI; pathfinder for long-baseline sensors, [arXiv:2104.02835](#).
- [50] S. G. Turyshev, S.-w. Chiow, and N. Yu, Searching for New Physics in the Solar System with Tetrahedral Spacecraft Formations, [Phys. Rev. D](#) **109**, 084059 (2024), [arXiv:2404.02096 \[gr-qc\]](#).
- [51] European Space Agency, Euclid opens data treasure trove, offers glimpse of deep fields, https://www.esa.int/Science_Exploration/Space_Science/Euclid/Euclid_opens_data_treasure_trove_offers_glimpse_of_deep_fields (2025), press release, 19 March 2025.
- [52] E. Babichev and C. Deffayet, An Introduction to the Vainshtein Mechanism, [CQG](#) **30**, 184001 (2013).
- [53] S. G. Turyshev, [High-Precision Lunar Corner-Cube Retroreflectors: A Wave-Optics Perspective](#) (2025), [arXiv:2504.06409 \[physics.optics\]](#).
- [54] D. E. Smith, M. T. Zuber, X. Sun, G. A. Neumann, J. F. Cavanaugh, J. F. McGarry, and T. W. Zagwodzki, Two-Way Laser Link over Interplanetary Distance, [Science](#) **311**, 53 (2006).

- [55] NASA/JPL-Caltech, [Deep Space Optical Communications \(DSOC\)](#) (2024), milestones: 267 Mb/s at 19 million miles (Dec 11, 2023); 25 Mb/s at 140 million miles (Apr 8, 2024). Accessed 2025-08-27.
- [56] T. W. Murphy Jr., Lunar laser ranging: the millimeter challenge, [CQG](#) **29**, 184005 (2012).
- [57] M. Zhang, J. Müller, and L. Biskupek, Advantages of combining Lunar Laser Ranging and Differential Lunar Laser Ranging, [Astronomy & Astrophysics](#) **681**, A5 (2024).
- [58] S. G. Turyshev, M. Shao, and K. Nordtvedt, The Laser Astrometric Test of Relativity (LATOR) Mission, [CQG](#) **21**, 2773 (2004), [arXiv:gr-qc/0311020](#).
- [59] S. G. Turyshev, M. Shao, and K. Nordtvedt, Mission design for the laser astrometric test of relativity, [Adv. Space Res.](#) **39**, 297 (2007), [gr-qc/0409111](#).
- [60] S. G. Turyshev, M. Shao, A. Gierd, and B. Lane, Search for New Physics with the Beacon Mission, [IJMPD](#) **18**, 1025 (2009), [arXiv:0805.4033 \[gr-qc\]](#).
- [61] J. D. Bekenstein, Relation Between Physical and Gravitational Geometry, [Phys. Rev. D](#) **48**, 3641 (1993).
- [62] T. S. Koivisto, D. F. Mota, and M. Zumalacárregui, Screening Modifications of Gravity Through Disformally Coupled Fields, [Phys. Rev. Lett.](#) **109**, 241102 (2012).
- [63] P. Brax, C. Burrage, A.-C. Davis, and G. Gubitosi, Cosmological Tests of the Disformal Coupling to Radiation, [JCAP](#) **2013** (11), 001.
- [64] J. Sakstein, Disformal Theories of Gravity: From the Solar System to Cosmology, [JCAP](#) **2014** (12), 012.
- [65] P. Brax, C. Burrage, and A.-C. Davis, Gravitational Effects of Disformal Couplings, [Phys. Rev. D](#) **98**, 063531 (2018).
- [66] A. Chakraborty, P. K. Chanda, S. Das, and K. Dutta, [DESI results: Hint towards coupled dark matter and dark energy](#) (2025), [arXiv:2503.10806 \[astro-ph.CO\]](#).

Appendix A: Beyond universal conformal couplings: disformal terms

A general matter metric may include a disformal term,

$$\tilde{g}_{\mu\nu} = C(\phi) g_{\mu\nu} + D(\phi) \partial_\mu \phi \partial_\nu \phi, \quad (\text{A1})$$

with $C(\phi) > 0$ and $D(\phi)$ analytic (see [61] for the original construction and [62] for “disformal screening.”) In the nonrelativistic limit around *static* sources, the disformal term does not generate a fifth force at leading order, so PPN bounds primarily constrain the conformal slope $C'(\phi_\star)/C(\phi_\star)$. However, for time-dependent backgrounds ($\dot{\phi} \neq 0$), disformal effects can enter light propagation and cosmology, modifying distance duality and CMB spectral distortions, and inducing Solar-System signatures suppressed by $\dot{\phi}$ (see [63–65].) Our guardrails extend verbatim: (i) impose EEP/PPN nulls; (ii) map DESI/Euclid posteriors on $\mu(z, k), \Sigma(z, k)$ to $\{C(\phi), D(\phi)\}$ consistent with $c_T \simeq c$; (iii) pursue dedicated Solar-System tests only when a specified $\{C, D\}$ predicts at least one local residual above credible thresholds.

Appendix B: A toy joint-likelihood across regimes

Let θ denote cosmology-level MG parameters (e.g., $\theta = \{\mu_0, \Sigma_0\}$) with posterior

$$p(\theta|C) \propto \exp\left[-\frac{1}{2}(\theta - \bar{\theta})^\top \mathbf{C}_C^{-1} (\theta - \bar{\theta})\right]. \quad (\text{B1})$$

Let $r(\theta)$ be a local residual (e.g., $r = \gamma - 1$) predicted via the screening map of Sec. II (thin shell or Vainshtein). Given a Solar-System measurement d_S with covariance \mathbf{C}_S , define

$$p(d_S|\theta) \propto \exp\left[-\frac{1}{2}(d_S - r(\theta))^\top \mathbf{C}_S^{-1} (d_S - r(\theta))\right]. \quad (\text{B2})$$

The joint posterior is

$$p(\theta|C, S) \propto p(\theta|C) p(d_S|\theta). \quad (\text{B3})$$

For small excursions one may linearize $r(\theta) \simeq r(\bar{\theta}) + \mathbf{J}(\theta - \bar{\theta})$ with Jacobian \mathbf{J} , which yields a closed-form Gaussian update of $\bar{\theta}$ and covariance. A null Solar-System result tightens θ along the rows of \mathbf{J} ; a detection triggers a non-linear refit with the same microphysical parameterization.

Appendix C: Reproducibility recipe (cosmology \rightarrow Solar-System)

Here we present a recipe on how to relate cosmological conditions to those of the Solar-System:

TABLE IX. Quick-look thin-shell bounds at the Sun for representative μ_0^{lin} and $|\gamma - 1|_{\text{max}}$, using $(\Delta R/R)_{\text{max}} = (1/3\chi)\sqrt{|\gamma - 1|_{\text{max}}/2}$ with $\chi = \sqrt{\mu_0^{\text{lin}}/2}$.

μ_0^{lin}	χ	$ \gamma - 1 _{\text{max}}$	$(\Delta R/R)_{\text{max}}$
0.05	0.1581	1×10^{-6}	1.49×10^{-3}
0.05	0.1581	5×10^{-6}	3.33×10^{-3}
0.10	0.2236	1×10^{-6}	1.05×10^{-3}
0.10	0.2236	5×10^{-6}	2.36×10^{-3}
0.15	0.2739	1×10^{-6}	8.61×10^{-4}
0.15	0.2739	5×10^{-6}	1.92×10^{-3}

1. Pick a linear-response parameter $\mu_0^{\text{lin}} \equiv \mu(z=0, k \sim 0.1 h \text{ Mpc}^{-1}) - 1$ and map to the local coupling via $\chi \simeq \sqrt{\mu_0^{\text{lin}}/2}$ (unscreened limit).
2. For chameleon-like models with $V(\phi) = \Lambda^{4+n}\phi^{-n}$ and $A(\phi) = e^{\chi\phi/M_{\text{Pl}}}$, compute the density minimum using

$$\phi_*(\rho) = \left(\frac{n \Lambda^{4+n} M_{\text{Pl}}}{\chi \rho} \right)^{1/(n+1)} \quad [\text{Eq. (3)}].$$

3. In the Sun-screened regime ($\rho_c \gg \rho_\infty$), use

$$\frac{\Delta R}{R} \simeq \frac{\phi_*(\rho_\infty)}{6 \chi M_{\text{Pl}} \Phi_{N\odot}} \quad [\text{Eqs. (2), (7)}].$$

4. Translate a null Shapiro test at sensitivity $|\gamma - 1|_{\text{max}}$ into the thin-shell requirement

$$\frac{\Delta R}{R} \lesssim \frac{1}{3\chi} \sqrt{\frac{|\gamma - 1|_{\text{max}}}{2}},$$

valid when the solar source is screened.

Appendix D: Sun thin shell and PPN γ for $(n, \chi) = (0.16, 0.28)$

This section considers the Sun thin-shell fraction $\Delta R/R$ and the associated PPN deviation $\gamma - 1$ for the *illustrative* choice $(n, \chi) = (0.16, 0.28)$ using the framework defined in Secs. II–IV, considering the low n scenarios [66]. We refer to the thin-shell relation and density minimum in Eqs. (2) and (3), the Sun’s surface potential in Eq. (7)/Table I, the γ -shell map in Eq. (22), and the null-test guardrail in Eq. (23). The ambient-density prior along a solar-conjunction ray is summarized in Table III. Starting from (2) and (3),

$$\frac{\Delta R}{R} \simeq \frac{\phi_\infty - \phi_c}{6 \chi M_{\text{Pl}} \Phi_N}, \quad \phi_*(\rho) = \left(\frac{n \Lambda^{4+n} M_{\text{Pl}}}{\chi \rho} \right)^{\frac{1}{n+1}}, \quad (\text{D1})$$

we fix the cosmological normalization by requiring $V(\phi_*(\rho_{\text{cos}})) = \rho_{\text{DE}}$ for the power-law potential $V(\phi) = \Lambda^{4+n}\phi^{-n}$. Using $V'(\phi_*) + \rho_{\text{cos}} A'(\phi_*) = 0$ one obtains

$$\Lambda^{4+n} = \rho_{\text{DE}}^{n+1} n^n M_{\text{Pl}}^n (\chi \rho_{\text{cos}})^{-n}. \quad (\text{D2})$$

In the screened-Sun limit ($\phi_c \ll \phi_\infty$), $\Delta R/R \simeq \phi_*(\rho_\infty)/(6\chi M_{\text{Pl}} \Phi_N)$. Substituting (D2) into $\phi_*(\rho_\infty)$ yields the closed form

$$\frac{\Delta R}{R} = \frac{n}{6 \chi^2 \Phi_N} \frac{\rho_{\text{DE}}}{\rho_{\text{cos}}^{n/(n+1)} \rho_\infty^{1/(n+1)}}. \quad (\text{D3})$$

For $\rho_{\text{cos}} = \rho_{\text{DE}}$ this reduces to

$$\frac{\Delta R}{R} = \frac{n}{6 \chi^2 \Phi_N} \left(\frac{\rho_{\text{DE}}}{\rho_\infty} \right)^{1/(n+1)}, \quad (\text{D4})$$

which makes the $\rho_\infty^{-1/(n+1)}$ scaling explicit, consistent with Table III.

The Sun-sourced PPN mapping used in the main text is (22), repeated here for convenience:

$$|\gamma - 1| \simeq 18\chi^2 \left(\frac{\Delta R}{R} \right)^2. \quad (\text{D5})$$

In the small-coupling limit one has $\gamma - 1 \simeq -2\alpha_\odot^2$; we thus compare to data using $|\gamma - 1| = 2\alpha_\odot^2$ throughout.

Numerical surface potentials needed below are given in Table I. We adopt $\Phi_{N\odot} = 2.12 \times 10^{-6}$ as per Eq. (7) and Table I, $(n, \chi) = (0.16, 0.28)$, $\rho_{\text{DE}} = 10^{-29} \text{ g cm}^{-3}$, and the near-conjunction ambient-density prior given as $\rho_\infty \in [10^{-22}, 10^{-19}] \text{ g cm}^{-3}$ (Table III). With $\rho_{\text{cos}} = \rho_{\text{DE}}$, Eq. (D4) gives, for the central choice $\rho_\infty = 10^{-20} \text{ g cm}^{-3}$,

$$\frac{\Delta R}{R} = \frac{0.16}{\underbrace{6(0.28)^2(2.12 \times 10^{-6})}_{1.604 \times 10^5}} (10^{-9})^{1/(1+0.16)} = 2.80 \times 10^{-3}, \quad (\text{D6})$$

$$\gamma - 1 = 18(0.28)^2 (2.80 \times 10^{-3})^2 = 1.10 \times 10^{-5}. \quad (\text{D7})$$

Across the prior range of ρ_∞ used in the paper (Table III; “a few R_\odot ” along the conjunction ray),

$$\begin{aligned} \rho_\infty = 10^{-22} \text{ g cm}^{-3} : \Delta R/R &= 1.482 \times 10^{-1}, \quad \gamma - 1 = 3.10 \times 10^{-2}, \\ \rho_\infty = 10^{-19} \text{ g cm}^{-3} : \Delta R/R &= 3.842 \times 10^{-4}, \quad \gamma - 1 = 2.08 \times 10^{-7}. \end{aligned}$$

The thin-shell approximation requires $\Delta R/R \ll 1$; when this fails, the screened-source premise is not satisfied and such points are excluded by Solar-System bounds.

Using Eq. (22), the null-test guardrail Eq. (23) is

$$\left(\frac{\Delta R}{R} \right)_{\text{max}} = \frac{1}{3\chi} \sqrt{\frac{|\gamma - 1|_{\text{max}}}{2}}. \quad (\text{D8})$$

For $\chi = 0.28$,

$$\begin{aligned} |\gamma - 1|_{\text{max}} = 2.3 \times 10^{-5} \text{ (Cassini, Eq. (14))} : (\Delta R/R)_{\text{max}} &= 4.04 \times 10^{-3}, \\ |\gamma - 1|_{\text{max}} = 5 \times 10^{-6} : (\Delta R/R)_{\text{max}} &= 1.88 \times 10^{-3}, \\ |\gamma - 1|_{\text{max}} = 1 \times 10^{-6} : (\Delta R/R)_{\text{max}} &= 8.42 \times 10^{-4}. \end{aligned}$$

Our central result $\Delta R/R = 2.80 \times 10^{-3}$ (at $\rho_\infty = 10^{-20} \text{ g cm}^{-3}$) is *below* the Cassini bound and consistent with the mapping shown in Fig. 2.